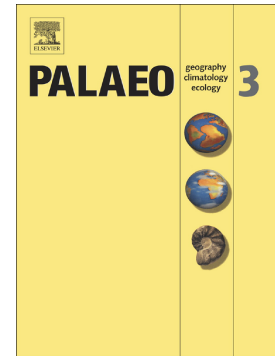


Accepted Manuscript

Volcanic and hydrothermal activities recorded in phosphate nodules from the Lower Cambrian Niutitang Formation black shales in South China

Ping Gao, Zhiliang He, Shuangjian Li, Gary G. Lash, Boyuan Li, Boyu Huang, Detian Yan



PII: S0031-0182(17)31156-2
DOI: doi:[10.1016/j.palaeo.2018.06.019](https://doi.org/10.1016/j.palaeo.2018.06.019)
Reference: PALAEO 8824

To appear in: *Palaeogeography, Palaeoclimatology, Palaeoecology*

Received date: 12 November 2017
Revised date: 9 June 2018
Accepted date: 9 June 2018

Please cite this article as: Ping Gao, Zhiliang He, Shuangjian Li, Gary G. Lash, Boyuan Li, Boyu Huang, Detian Yan , Volcanic and hydrothermal activities recorded in phosphate nodules from the Lower Cambrian Niutitang Formation black shales in South China. *Palaeo* (2018), doi:[10.1016/j.palaeo.2018.06.019](https://doi.org/10.1016/j.palaeo.2018.06.019)

This is a PDF file of an unedited manuscript that has been accepted for publication. As a service to our customers we are providing this early version of the manuscript. The manuscript will undergo copyediting, typesetting, and review of the resulting proof before it is published in its final form. Please note that during the production process errors may be discovered which could affect the content, and all legal disclaimers that apply to the journal pertain.

Volcanic and hydrothermal activities recorded in phosphate nodules from the Lower Cambrian Niutitang Formation black shales in South China

Ping Gao^a, Zhiliang He^a, Shuangjian Li^a, Gary G. Lash^b, Boyuan Li^c, Boyu Huang^c, Detian Yan^{d*}

^a, Petroleum Exploration & Production Research Institute, SINOPEC, Beijing 100083, China

^b, Department of Geology and Environmental Sciences, State University of New York - Fredonia, Fredonia, NY 14063, USA

^c, State Key Laboratory of Petroleum Resources and Prospecting, China University of Petroleum, Beijing 102249, China

^d, Key Laboratory of Tectonics and Petroleum Resources of Ministry of Education, China University of Geosciences, Wuhan 430074, China

*Corresponding author, Tel.: +86-27-67883051, E-mail: yandetian@cug.edu.cn;

gaoping1212@hotmail.com

Abstract: Deposition of black shale of the Lower Cambrian Niutitang Formation (NTT) of the Yangtze Block, South China, in association with the Ediacaran-Cambrian (E-C) transition was accompanied by widespread formation of phosphate nodules. Petrological and geochemical studies of the nodules and host sedimentary rocks were carried out to elucidate hydrographic conditions of the Early Cambrian ocean. Our results reveal that NTT phosphate nodules are composed principally of concentrically banded carbonate fluorapatite (CFA) that likely reflects changing Eh and pH conditions contemporaneous with diagenetic nodule growth. Accumulation of organic-rich sediment and nodule growth may have been induced and sustained by contemporaneous volcanic

and hydrothermal activities on the Yangtze Block. The introduction of voluminous nutrients with volcanic ash, including phosphate and aqueous Fe and Si, promoted the bloom of plankton, including sponges and lower algae leading to organic matter enrichment. Productivity may have been further enhanced by upwelling of phosphate-rich bottom water that resulted in widespread phosphogenesis and formation of phosphate nodules. The hyalophane-quartz association documented from phosphate nodules suggests the possible interaction of K-feldspar-rich volcanic ash and Ba-rich hydrothermal fluids at lower pH levels in association with nodule growth. The formation of phosphate nodules of the Niutitang Formation, then, reflects the complex interaction among primary productivity, volcanic and hydrothermal activity, and the accumulation of organic matter at a critical period of Earth history.

Keywords: Carbonate fluorapatite; phosphogenesis; tuff; upwelling; organic matter

1. Introduction

The Ediacaran-Cambrian (E-C) transition is a major turning point in Earth history characterized by global environmental and biological changes, including the break-up of the supercontinent Rodinia (Li et al., 2008), the establishment of anoxic or even sulfidic bottom-water conditions (Kimura and Watanabe, 2001; Och et al., 2013; Pi et al., 2013; Gao et al., 2016; Cheng et al., 2016, 2017; Zhang et al., 2017; Yeasmin et al., 2017), the stepwise oxygenation of the global ocean (Scott et al., 2008; Jin et al., 2016), and subsequent Cambrian radiation of animals (Steiner et al., 2007; Li et al., 2017). Lower Cambrian black shale deposits that host chert, phosphorite, and Ni-Mo

polymetallic ore, widely distributed across the Yangtze Block provide a unique opportunity to investigate the evolving oceanic environment at this critical period of Earth history (Goldberg et al., 2007; Jiang et al., 2007; Steiner et al., 2001, 2007; Och et al., 2013; Pi et al., 2013; Gao et al., 2016; Cheng et al., 2016, 2017; Li et al., 2017).

Phosphorites and phosphate nodules are widely developed in modern and ancient marine sediments (Baturin, 1982; Föllmi, 1996; Nelson et al., 2010; Dabard and Loi, 2012). Modern phosphorites are most common to continental shelf and shelf sites that have experienced upwelling, including the Gulf of California, Chile, Peru, and Namibia (Baturin, 1982; Froelich et al., 1988; Föllmi, 1996). Similarly, ancient phosphorites reported from various sedimentary facies and paleogeographic locations (Nelson et al., 2010; Dabard and Loi, 2012; She et al., 2013), have been linked to enhanced biological productivity, perhaps fueled by upwelling of nutrient-rich bottom water (Föllmi, 1996; Shen et al., 2000; Nelson et al., 2010; She et al., 2013; Li and Schieber, 2015; Muscente et al., 2015).

Phosphorite deposits and phosphate nodules are commonly associated with slowly deposited transgressive system tract and immediately overlying highstand system tract deposits, especially condensed black shale successions (Jiang et al., 2007; Loi et al., 2010; Nelson et al., 2010; Dabard and Loi, 2012; Zhu et al., 2014; Li and Schieber, 2015; Muscente et al., 2015). Low sedimentation rates stabilize diagenetic zones within the sediment column for protracted periods of time (Dabard and Loi, 2012; Muscente et al., 2015) favoring the growth of nodules. The connection of phosphate nodule formation and episodes of markedly diminished sedimentation/burial rate demonstrate

the potential use of nodule intervals for correlation of sea (base) level fluctuations. Phosphate nodules can also form in response to hydrothermal (Zhu et al., 2014; Zhu and Jiang, 2017) and submarine volcanic activities (Berner, 1973). The range of conditions under which phosphate nodules may make them especially useful for deciphering depositional conditions and diagenetic modification of the host sediment (e.g., Shields and Stille, 2001; Kidder et al., 2003; Jiang et al., 2007; Dabard and Loi, 2012; Zhu et al., 2014; Li and Schieber, 2015; Xin et al., 2015; Zhu and Jiang, 2017). The present study considers the conditions under which phosphate nodules of the Lower Cambrian Niutitang Formation of the Yangtze Block, South China, formed during the E-C transition. We present results of a comprehensive integrated study of these deposits based on petrological and geochemical investigation.

2. Geological setting and sampled section

The major geologic elements of South China include the Yangtze and Cathaysia blocks (Fig.1). The former comprises three Lower Cambrian sedimentary facies, including carbonate platform, transitional, and slope-basinal facies from northwest to southeast (Fig.1; Chen et al., 2009; Gao et al., 2016). The Rongxi section, the focus of the present study, is located ~14 km northwest of Xiushan City in Chongqing Province (Fig. 1). Early Cambrian paleogeographic reconstruction suggests that Rongxi section was located in the transitional belt of Yangtze Block (Guo et al., 2007; Steiner et al., 2007).

Figure 1 Near here

The Lower Cambrian Niutitang Formation (NTT) of the Rongxi section rests unconformably on dolomite deposits of the Dengying Formation, which consists principally of black siliceous shale, bedded chert, tuff, and black shale, in ascending order (Fig. 2 and 3). Phosphate nodules are most common to the lower part of the NTT black shales overlying conspicuous tuff and chert layers (Fig. 2 and 3). At least three tuff layers have been documented from within the phosphatic succession of the Early Cambrian Meishucun Stage on the carbonate platform of South China (Compston et al. 2008). A tuff layer (Bed 5) in the Zhongyicun Member of the Meishucun section has been dated in multiple studies using zircon SHRIMP U-Pb method as 538.2 ± 1.5 Ma (Jenkins et al., 2002), 536.5 ± 2.5 Ma (Sawaki et al., 2008), 539.4 ± 2.9 Ma (Compston et al., 2008), and 535.2 ± 1.7 Ma (Zhu et al., 2009) (Fig. 2). The tuff layer above the Liuchapo chert in the Ganziping section has yielded an age of 536.3 ± 5.5 Ma (Chen et al., 2009). A tuff layer about 5 m below the Ni-Mo horizon of the Zhongnancun section (Pi et al., 2013) has a U-Pb age of 532.3 ± 0.7 Ma (Jiang et al., 2009). Compston et al. (2008) report a younger U-Pb age of 526.5 ± 1.1 Ma for a tuff layer within the basal Shiyantou Member (Bed 9) of the Meishucun section (Fig. 2). Dating of the Ni-Mo ore layer below which phosphate nodules and associated phosphorite deposits of South China have been observed (Steiner et al., 2001; Zhu et al., 2009; Pi et al., 2013; Jin et al., 2016) by the Re-Os method yields an age of 521 ± 5 Ma (Xu et al., 2011). Thus, the age of the NTT phosphate nodules can be constrained between 538 and 521 Ma (Fig. 2).

Marine deposits of the Yangtze Block preserve the record of a transgressive-regressive cycle that spanned the Fortunian to Cambrian Stage 3 (Goldberg et al., 2007; Wang et al., 2015; Yeasmin et al., 2017). The Fortunian transgression on the Yangtze Platform was dominated by carbonate and phosphorite deposition. A thin condensed succession that includes chert, black shale, and phosphatic nodules accumulated slowly in the adjacent slope-basin area (Steiner, 2001). Transgression continued into Cambrian Stage 2 time and was accompanied by widespread deposition of the NTT black shale, including the studied phosphate nodules in its basal part (Goldberg et al., 2007; Steiner et al., 2007) (Fig. 2). Overlying deposits reflect marine regression that persisted into the early part of Cambrian Stage 3 time (Wang et al., 2015; Yeasmin et al., 2017).

Figure 2 Near here

Figure 3 Near here

3. Samples and analytical methods

3.1. Samples

Six phosphate nodule samples and eleven host rock samples were collected from the Rongxi section at an abandoned phosphorite mine (Fig. 2 and 3). Detail information of the samples is provided in Table 1. All samples were ground to a 200 mesh size in an automatic agate mortar.

Table 1 Near here

3.2 Analytical methods

Optical observation of polished thin sections of nodule samples was performed on a Zeiss Axioskop 40 A pol microscope. Thin sections were then coated with platinum for analysis using a Carl Zeiss EVO MA10 scanning electron microscope (SEM) equipped with INCAx-sight electron dispersive X-ray dispersive spectroscopy (EDS) system detector (Oxford Instruments, UK) for imaging at backscatter electron (BSE) mode at 20 kV. Optical investigations were conducted at the Laboratory of Structural and Sedimentological Reservoir Geology, Sinopec.

Carbonate was removed from powdered samples with dilute HCl after which total organic carbon (TOC) and total sulfur (TS) contents were measured using a Leco CS-230 analyzer. Analytical precision was better than 10 %. This work was conducted at the State Key Laboratory of Petroleum Resources and Prospecting of the China University of Petroleum (SKLPRP-CUP), Beijing. X-ray diffraction (XRD) measurements of powdered samples were conducted at the Microstructure Laboratory for Energy Materials of CUP using a Bruker D8 Advance diffractometer.

Major, trace, and rare earth element (REE) concentrations were measured at the Analytical Laboratory of the Beijing Research Institute of Uranium Geology. Major oxides of host rocks were determined on a Philips PW2404 X-ray fluorescence analyzer on fusion glasses of a 1:10 ratio of sample to $\text{Li}_2\text{B}_4\text{O}_7$ in accordance with Ma et al. (2015). Major element (Fe, Al, K, Na, Ca, Mg) concentrations of phosphate nodules

were determined on a PerkinElmer 5300DV ICP-OES using sample powders digested in a mixture of super-pure HNO₃+HCl+HF in high-pressure Teflon cups as outlined by Gao et al. (2016). Trace and REE concentrations of all samples were determined on a PerkinElmer NexION300D ICP-MS using sample powders digested as per above. Analytical precision was better than 5 % for major and trace elements and 10 % for REE. Enrichment factors (EFs) were calculated as $X\text{-EF} = [(X/Al)_{\text{sample}} / (X/Al)_{\text{PAAS}}]$, where X and Al represent weight percent concentrations of elements X and Al of the sample and the Post-Archean Australian Shale (PAAS) standard (Taylor and McLennan, 1985). Ce, Eu, and Pr anomalies were calculated according to Shields and Stille (2001); i.e., $Ce/Ce^* = 3Ce_N / (2La_N + Nd_N)$, $Eu/Eu^* = Eu_N / (Sm_N \times Gd_N)^{1/2}$ and $Pr/Pr^* = 2Pr_N / (Ce_N + Nd_N)$, where N refers to elemental concentrations normalized to PAAS (McLennan, 1989).

4. Results

4.1. Petrological and mineralogical features

4.1.1. Phosphate nodules

NTT phosphate nodules display a variety of shapes, including globular, ovoid, and oblate, and range from 0.2 to 5.0 cm in diameter. Nodules are wrapped by microlaminations of host shale suggesting that they formed early in the diagenetic history of these deposits prior to sediment compaction. XRD analysis reveals NTT phosphate nodules to be composed mainly of carbonate fluorapatite (CFA) and subordinate quartz and hyalophane (Fig. 4A). Further, optical and SEM observations reveal a concentrically layered internal structure (Fig. 5A and Fig. 6A, B).

Figure 4 Near here

Nodule cores are dominated by crystalline CFA (Fig. 7A, B) which exhibits optical characteristics similar to quartz under cross-polarized light (Fig. 5A). Solid bitumen (SB) is concentrated along edges of crystalline CFA (Fig. 6C). Crystalline CFA is accompanied by lesser cryptocrystalline CFA and accessory amounts of pyrite and hyalophane (Fig. 6C). The first layer outward from nodule cores is composed mostly of cryptocrystalline CFA (Fig. 6A) which exhibits total optical extinction under cross-polarized light (Fig. 5A). The following layer comprises quartz, hyalophane, and subordinate K-feldspar (Fig. 6A, D-F and Fig. 7C, E). The elemental composition of hyalophane ((K,Ba)Al₂Si₂O₈; Frondel et al., 1966) is evident in EDS spectra (Fig. 7D and Table 2) and XRD patterns (Fig. 4A). Hyalophane observed in the present study appears to be relatively enriched in Ba and depleted of K (Table 2). We are not aware of other reported occurrences of hyalophane in phosphate nodules. Sponge spicules, walled by CFA and quartz (Fig. 6E, F) and filled with solid bitumen (SB), have been observed in this layer. The outer layer of studied nodules is compositionally similar to the first layer, i.e., dominated by cryptocrystalline CFA (Fig. 6B). Solid bitumen present in this layer displays various morphologies, including spherical, elliptical, and rod-like. It is also observed as amorphous material, some of which appears to fill sponge spicules. The walls of these microfossils are composed of CFA and occasional trace amounts of hyalophane (Fig. 6H) and pyrite.

Table 2 Near here

Figure 5 Near here

Figure 6 Near here

Figure 7 Near here

4.1.2. Host and associated rocks

The phosphate nodule layer is underlain by a tuff layer (Fig. 3) comprised chiefly of muscovite, quartz, and hyalophane and lesser CFA, gypsum, albite, K-feldspar and pyrite (Fig. 4C). These deposits overlie a phosphorite layer (Fig. 3) composed principally of CFA and quartz and subordinate gypsum, muscovite, albite, and hyalophane (Fig. 4B). Phosphate nodules are hosted by black shale (Fig. 3) consisting of quartz, muscovite, gypsum, albite, and CFA (Fig. 4D).

4.2. Bulk organic geochemistry

The studied phosphate nodules are carbon-rich with TOC values ranging from 7.9 to 9.1 % (average = 8.6 %; n = 6) (Table 1). Total sulfur (TS) of the nodules is low, varying from 0.09 to 0.2 % (average = 0.1 %; n = 6) (Table 1). Chert, phosphorite, and tuff are characterized by low TOC (0.5-1.9 %) and TS (0.04-0.5 %), whereas black shale samples are enriched in organic carbon (TOC = 4.8-18 %; average = 10 %; n = 9)

and sulfur (TS = 0.2-3.2 %; average = 1.3 %; n = 9).

4.3. Element geochemistry

4.3.1. Major elements

Phosphate nodules display elemental and oxide concentrations of Fe, Al, K, Na and Mg of less than 1 %, but are markedly enriched in Ca, containing more than 30 %. Major oxide concentrations of associated rocks are quite variable (Tables 3 and 4). As expected, chert is dominated by SiO₂ (96.2 %) (Tables 3 and 4). The dominant oxides of the phosphorite include CaO (30.3 %), SiO₂ (29.9 %), and P₂O₅ (22.1 %) (Table 3 and 4). Tuff is dominated by SiO₂ (43.7 %) and Al₂O₃ (22.7 %) (Tables 3 and 4). The tuff sample contains 5.4 % K₂O, strongly enriched relative to PAAS and close to values documented from K-bentonite associated with the Lower Cambrian black rock series of South China (Zhou et al., 2007). The dominant major element oxides of analyzed black shale samples are SiO₂ (37.0 to 54.4 %) and Al₂O₃ (3.8 % to 12.1 %) (Table 3 and 4). It is noteworthy that these deposits are enriched in P₂O₅ relative to PAAS.

Table 3 Near here

Table 4 Near here

4.3.2. Trace and rare earth elements

NTT phosphate nodules display high concentrations of redox-sensitive trace elements and metals, notably V, Mo, and U. Moreover, analyzed nodule samples are

enriched in Ba relative to PAAS (McLennan, 1989) (Table 5). Concentrations of redox-sensitive metals (e.g., V, Mo, Ni) in the host rocks are 10-100 times higher than in phosphate nodules. It is worth noting that the tuff and black shales are characterized by abnormally high concentrations of Ba, ranging from 4,000 to 46,500 ppm (Table 5).

Table 5 Near here

NTT phosphate nodules and the phosphorite sample display the highest total REE contents ($\Sigma\text{REE} > 500\text{ppm}$) of the Rongxi section sample suite (Table 6). The tuff and black shale samples are characterized by ΣREE values ranging from 94.1 to 362 ppm, and the chert samples is markedly depleted of ΣREE (Table 6). REE concentrations of NTT phosphate nodules normalized to PAAS exhibit a convex-upward pattern with pronounced negative Ce anomalies ($\text{Ce}/\text{Ce}^* = 0.39\text{-}0.46$), slightly positive Eu anomalies ($\text{Eu}/\text{Eu}^* = 1.00\text{-}1.25$), and higher Y/Ho ratios (44.2-49.2) (Fig. 8A). Host and associated rocks display generally diminishing values from low to high atomic numbers as well as moderate negative Ce anomalies ($\text{Ce}/\text{Ce}^* = 0.36\text{-}0.78$), slightly positive Eu anomalies ($\text{Eu}/\text{Eu}^* = 1.11\text{-}2.07$ with the exception of the single negative Eu anomaly associated with the chert sample), and lower Y/Ho ratios (34.0-46.8) (Fig. 8B).

Table 6 Near here

Figure 8 Near here

5. Discussion

5.1. Oceanic conditions during Early Cambrian time

5.1.1. Redox conditions

Redox-sensitive trace elements, notably U, V and Mo, are considered especially useful to paleoenvironmental reconstruction of sediment that accumulated under oxygen-deficient and/or sulfidic bottom-water conditions (Algeo and Maynard, 2004; Algeo and Lyons, 2006; Algeo and Rowe, 2012; Tribovillard et al., 2009; Scott and Lyons, 2012). Absolute concentrations and enrichment factors of these elements as well as their degrees of co-variance with TOC have been used to elucidate redox conditions (Algeo and Maynard, 2004; Algeo and Lyons, 2006; Tribovillard et al., 2009; Scott and Lyons, 2012; Pi et al., 2013). Mo concentrations of analyzed NTT black shale samples (30.8-329 ppm; average = 151 ppm; n = 8) suggest deposition under at least intermittently euxinic conditions (Scott and Lyons, 2012). Mo concentrations of chert, phospharite and tuff samples of less than 25 ppm (Fig. 9) indicate non-euxinic conditions though porewater may have contained sulfide (Scott and Lyons, 2012).

Figure 9 Near here

Mo-TOC relationships serves as an independent means of discerning bottom water redox conditions (Algeo and Maynard, 2004; Algeo and Lyons, 2006; Tribovillard et

al., 2006; Pi et al., 2013). Organic-rich shale deposited under anoxic bottom conditions generally exhibit modest Mo enrichment and strong TOC-Mo covariation owing to Mo residence primarily in organic phases (Algeo and Maynard, 2004). However, strong Mo enrichment and weak TOC-Mo covariation documented from black shale deposited under euxinic conditions reflect the concentration of Mo in authigenic sulfide or oxyhydroxide phases (Algeo and Maynard, 2004). The weak correlation of Mo and Al abundances of the NTT black shale samples (Fig. 10A) indicate that Mo was scavenged from seawater rather than supplied with the detrital flux. Moreover, elevated Mo/Al ratios of these deposits display a moderate negative correlation with TOC (correlation coefficient (R) = -0.45, $P(\alpha) > 0.05$, $n = 8$; Fig. 10B) suggesting deposition under euxinic conditions (Algeo and Maynard, 2004). Interestingly, the single chert sample is strongly enriched in Mo indicating anoxic conditions whereas the phosphorite and tuff samples, by virtue of their low Mo concentrations appear to reflect deposition under oxic-suboxic conditions (Algeo and Maynard, 2004) (Fig. 10B).

Figure 10 Near here

Algeo and Tribovillard (2009) and Tribovillard et al. (2012) described the use of patterns of authigenic U and Mo covariation as a means of discriminating redox conditions of diverse marine depositional systems. Mo-EF values generally mimic the trend of increasing Mo concentration upward through the Rongxi section (Fig. 9). Uranium, though enriched through the studied section, does not display increasing

enrichment up-section (Fig. 9). Most black shale samples are characterized by $(\text{Mo}/\text{U})_{\text{auth}}$ ratios 1 to 3 times that of modern seawater (Fig. 11), suggestive of anoxic-euxinic bottom water conditions in an open marine environment (Algeo and Tribovillard, 2009). Therefore, anoxic-euxinic bottom water conditions appear to have prevailed during deposition of NTT black shale and chert, perhaps becoming more strongly euxinic over time.

Figure 11 Near here

5.1.2. Primary productivity

A variety of geochemical proxies have been employed to reconstruct past changes in primary productivity, including C and N isotopes, organic biomarkers, TOC, and trace metal (Ba, P, Cu, Ni, Cd, Zn) abundances (Paytan and Griffith, 2007; Tribovillard et al., 2006; Schoepfer et al., 2015; Shen et al., 2015; Liu et al., 2015). Among them, TOC, organic phosphorus (P_{org}) and biogenic barium (B_{bio}) are the most widely used for reconstructing primary productivity in both modern and ancient sediments (Schoepfer et al., 2015; Shen et al., 2015). Moreover, the use of elements that behave as micronutrients (Cu, Zn, and Ni) is also finding greater use as productivity proxies (Liu et al., 2015; Tribovillard et al., 2006). As no single proxy is inherently more reliable than others, primary productivity assessments should be made based on the covariation of multiple proxies (Paytan and Griffith, 2007; Schoepfer et al., 2015).

Strong positive co-variance among TOC, P, and Cu abundances of the studied NTT samples ($R = +0.67$, $P(\alpha) < 0.05$, $n = 10$ for TOC vs. Cu, exclusive of the tuff sample; $R = +0.67$, $P(\alpha) < 0.05$, $n = 9$ for TOC vs. P, exclusive of the tuff and phosphorite samples; $R = +0.70$, $P(\alpha) < 0.05$, $n = 9$ for Cu vs. P, exclusive of tuff and phosphorite samples) demonstrates their potential as primary productivity proxies. Organic carbon content is perhaps the most direct proxy of productivity (Pedersen and Calvert, 1990), yet a substantial portion of organic matter (OM) is lost during transportation to the sea floor and burial processes (Froelich et al., 1979). Thus, measured TOC values reflect the combined effects of primary surface water productivity, and OM preservation within the water column and during burial (Schoepfer et al., 2015; Shen et al., 2015). Organic P is calculated by the following relationship: $P_{org} = P_{total} - Al \times (P/Al)_{detr}$, in which P_{total} is the total P of the sample and $(P/Al)_{detr}$ is the Al-normalized detrital P content. Similarly, biogenic Cu content is calculated as follows: $Cu_{bio} = Cu_{total} - Al \times (Cu/Al)_{detr}$. The $(P/Al)_{detr}$ and $(Cu/Al)_{detr}$ values are estimated from Al vs. P and Al vs. Cu crossplots in which the samples displaying the lowest P/Al and Cu/Al ratios are presumed to contain minimal biogenic P and Cu (Shen et al., 2015; Schoepfer et al., 2015). Application of this methodology to the present study yields a $(P/Al)_{detr}$ ratio of 0.0077 and a $(Cu/Al)_{detr}$ ratio of 0.0003. Cu_{bio} values of NTT black shale samples range from 12.1 to 145 ppm (average = 66.7 ppm, $n = 7$); the chert and phosphorite samples have moderate Cu_{bio} values of 26.2 ppm and 46.3 ppm, respectively. The elevated Cu_{bio} value of the tuff sample (135 ppm) probably reflects the presence of sulfides (e.g., pyrite; Fig. 4C) as Cu is mostly hosted by pyrite within sediments (Tribovillard et al., 2006). P_{org} values

of black shale vary from 0.004 to 2.8 % (average = 0.7 %; n = 7). As might be expected, P_{org} is greatest in the phosphorite samples (9.6 %) whereas chert and tuff display P_{org} values of 0.02 % and 1 %, respectively (Fig. 9).

Calculated Cu_{bio} and P_{org} values are normally elevated in highly productive upwelling zones of the modern ocean, ranging from 1.32 to 53.1 ppm (average = 24.9 ppm; n = 15) and 0.01 to 1.90 % (average = 0.27 %; n = 27), respectively (Murray and Leinen, 1993; Böning et al., 2004). Thus, Cu_{bio} and, to a lesser extent, P_{org} values of the NTT black shale compare favorably with sediment deposited beneath modern high productivity upwelling zones (Fig. 9). Moreover, P_{org} values of the NTT black shale and chert samples may be underestimations given the tendency of phosphate to recycle back to the water column under anoxic conditions (Föllmi, 1996; Algeo and Ingall, 2007; Nelson et al., 2010).

In summary, the studied shale interval appears to have accumulated beneath very productive surface water. Early Cambrian palaeogeographic reconstructions place the Yangtze Block in the Northern Hemisphere tropics (~5-25°N) (Steiner et al., 2007; Li et al., 2008). Modern phosphorite deposits are well-documented from areas of coastal upwelling in tropical regions (30°N-30°S) (Baturin, 1982; Föllmi, 1996). Thus, the Rongxi section, by virtue of its inferred paleogeographic position on the slope belt of Yangtze Block (Chen et al., 2009; Yeasmin et al., 2017), would have been favorably positioned to experience enhanced organic matter export induced by the upwelling of phosphate-enriched deep water thus favoring accumulation of phosphorites and P-rich black shales.

5.1.3. Possible impact of contemporaneous volcanic activity on OM enrichment

The inconsistent relationship of TOC, P_{org} and Cu_{bio} with inferred redox conditions based on Mo geochemistry and Mo-U covariation (compare Mo profiles with TOC profile, Fig. 9) suggests that OM enrichment was driven principally by productivity. It is worth noting that TOC of the black shale is most concentrated lower in the sequence, a short distance above and below the tuff layer (Fig. 9). The association of K-rich volcanic ash and NTT black shale of the Yangtze Block attests to the coincidence of volcanism and deposition of carbonaceous sediment during Early Cambrian time (Zhou et al., 2007 and this study). The possibility that volcanic eruptions may have enhanced surface water productivity finds support in the relatively strong positive co-variance of TOC and K among the studied samples, excluding the single tuff sample ($R = +0.81$, $P(\alpha) < 0.01$, $n = 10$; Fig. 12).

Figure 12 Near here

Modern volcanic eruptions are commonly accompanied by the release of biolimiting nutrients, including N, P, Si, Fe, and Zn, which can significantly elevate marine primary productivity in the photic zone (Baturin, 2003; Olgun et al., 2013). Indeed, Si, P, and Fe concentrations in a region of the Mediterranean Sea affected by volcanic ash fallout are 10-2,000 times higher than open ocean abundances (Olgun et al., 2013). Abundant sponge spicules in NTT phosphate nodules could be attributed to a bloom of silica-secreting organisms coincident with deposition of the host shale

perhaps driven by an abnormally high Si influx. Weak-moderate positive correlations of Si and K concentrations ($R = +0.47$, $P(\alpha) > 0.05$, $n = 10$; Fig. 13A) and Si abundance and TOC ($R = +0.32$, $P(\alpha) > 0.05$, $n = 10$; Fig. 13A) indicate that some Si may have been derived from volcanic ash. Fe concentration also displays a moderate positive covariance with TOC ($R = +0.46$, $P(\alpha) > 0.05$, $n = 10$; Fig. 13B) hinting of some role in the enhancement of productivity. The strong positive correlation of Fe and K abundances ($R = +0.63$, $P(\alpha) > 0.05$, $n = 10$; Fig. 13B) suggests that the increased supply of Fe may have been contributed by volcanic ash.

Figure 13 Near here

5.2. Phosphogenesis and possible sources of phosphate

The presence of phosphorites and phosphate nodules in a sedimentary deposit is generally attributed to the biological accumulation of phosphorous well in excess of that delivered from terrestrial sources (Shen et al., 2000; Nelson et al., 2010; She et al., 2013). High pore water phosphate concentration is a prerequisite for phosphogenesis. Indeed, apatite will form only if pore water is supersaturated with respect to apatite (Föllmi, 1996). Sequestration of P in sediment occurs in association with burial of OM, Fe-hydroxide (FeOOH), phosphatic skeletal material, and authigenic apatite (Föllmi, 1996; Algeo and Ingall, 2007; Nelson et al., 2010; Muscente et al., 2015). Prior to the ecological diversification of organisms with phosphatic skeletons, major sources of phosphate in pore waters included P desorbed from FeOOH and that released from OM

(She et al., 2013; Muscente et al., 2015). Redox conditions of bottom and pore water appear to exert strong control on the burial of P desorbed from FeOOH. Oxic conditions favor phosphate mineralization (Nelson et al., 2010) whereas anoxia induces the release of phosphate adsorbed onto FeOOH particulates to pore water and the water column (Algeo and Ingall, 2007; Muscente et al., 2015). The described redox-dependent mechanism accounts for the uptake and removal of phosphate across oxic-anoxic boundaries within the sediment column (Algeo and Ingall, 2007; Nelson et al., 2010). In addition, the burial and microbial decomposition of OM release considerable P to pore water, much of which diffuses into the overlying water column (Nelson et al., 2010). Nevertheless, some released organic P is retained in pore water to be precipitated as apatite. The organic-rich nature of the studied phosphate nodules (average TOC = 8.6 %) suggests that the delivery of phosphate was tied to the flux of OM.

It is generally recognized that the Neoproterozoic period witnessed a series of widespread phosphogenic events (Shen et al., 2000; She et al., 2013; Muscente et al., 2015). The end of Cryogenian glaciation was accompanied by a sharp increase of atmospheric CO₂ and consequent enhanced continental weathering (Planavsky et al., 2010; She et al., 2013). The increased riverborne flux of phosphate into the global ocean promoted a bloom of marine plankton (e.g., cyanobacteria; She et al., 2013; Gao et al., 2016) that resulted in widespread phosphogenesis, including in that region of the ocean represented by the Rongxi section. Though volcanic ash could have been a source of phosphate (e.g., Olgun et al., 2013) incorporated into NTT nodules and phosphorite beds, the weak negative correlation of P and K ($R = -0.28$, $P(\alpha) > 0.05$, $n = 11$) argues

against such a scenario.

Minimal co-variance of P with several detrital proxies (Al, Th, and Ti) rules out a strong flux of riverborne P. The strong positive correlation of P_2O_5 and $\sum REE$ concentrations in Ediacaran Doushantuo Formation phosphate nodules (Xin et al., 2015) suggests that REE are concentrated in the apatite fraction of nodules. Y/Ho ratios of NTT nodules (44.2 to 49.2) exceed freshwater values (approximately 27; Gromet et al., 1984; Taylor and McLennan, 1985) but are close to the lower range of modern seawater values (48 to 59; Nozaki et al., 1997). A large amount of sponge spicules, phosphatic skeletal material (Fig. 6F-H) and higher OM contents in the nodules suggests that phosphate was principally sourced in organic remains of marine plankton that had assimilated phosphate and REE from seawater.

5.3. Hyalophane-quartz association and hydrothermal activity

Hyalophane is a member of the feldspar group of tectosilicates and is considered to be a barium feldspar commonly described from low to medium-grade metamorphic and volcanic or magmatic systems as a substitution for feldspar minerals (Deer et al., 2001). It has also been identified in sedimentary exhalative (SEDEX)-type Pb-Zn or Ba-Zn deposits, including those of the Czech Republic (Křibek et al., 1996), Spain (Moro et al., 2001), South China (Han F. et al., 1993; Han S. et al., 2015), as well as Mississippi Valley (MVT)-type Pb-Zn deposits (e.g., Ireland; Riegler and McClenaghan, 2017). Irrespective of its host rock, the presence of hyalophane is usually attributed to alteration caused by Ba-rich hydrothermal fluids (Křibek et al., 1996; Han et al., 2015; Riegler and McClenaghan, 2017).

The presence of hyalophane in ore deposits is generally related to hydrothermally induced diagenetic alteration of K-feldspar (Croxford and Jephcott, 1972; Han F. et al., 1993; Křibek et al., 1996; Riegler and McClenaghan, 2017). For example, hyalophane and adularia in McArthur River lead-zinc-silver deposits, Northern Territory, Australia, generally restricted to tuff, tuffaceous shale, and ore bodies, has been attributed to the interaction of volcanic ash and high-salinity alkaline hot brines (Croxford and Jephcott, 1972). The hyalophane-quartz association is most strongly developed in the second layer of the studied NTT phosphate nodules (Fig. 6B). As stated earlier, the tuff layer of the Rongxi section is enriched in hyalophane (Fig. 4C; Tables 2 and 5). Associated phosphorite and black shale also contain hyalophane (Fig. 4B, D). The close association of hyalophane, K-feldspar, and quartz in the NTT phosphate nodules (Fig. 6E) suggests that K-feldspar may have been largely replaced by Ba²⁺ as per the following reaction:

$$2\text{KAlSi}_3\text{O}_8 \text{ (K-feldspar)} + \text{Ba}^{2+} = (\text{K, Ba})\text{Al}_2\text{Si}_2\text{O}_8 \text{ (Hyalophane)} + 2\text{K}^+ + 4\text{SiO}_2.$$

As stated above, the presence of hyalophane is generally attributed to Ba-rich hydrothermal fluids. Hydrothermal activity occurred widely across the Yangtze Block during Early Cambrian time and may have provided elevated fluxes of Si and Ba necessary for the formation of chert and barite (Chen et al., 2009). Hydrothermal activity may be evidenced by positive Eu anomalies (Steiner et al., 2001; Zhu and Jiang, 2017). Although NTT phosphate nodules and host rocks exhibit positive Eu anomalies (Fig. 9), one must be aware that such an anomaly may be a relict of Ba interference during ICP-MS measurement (Dulski, 1994; Shields and Stille, 2001; Jiang et al., 2007). Indeed, the strong positive co-variance of Eu and Ba concentrations of NTT phosphate

nodules ($R = +0.73$, $P(\alpha) > 0.05$, $n = 6$) may reflect Ba interference. However, the weak correlation of Eu and Ba of the host rocks ($R = +0.11$, $P(\alpha) > 0.05$, $n = 11$) suggests that the positive Eu anomalies are hydrothermal in origin. Moreover, the strong enrichment of NTT phosphate nodules and host black shale in Cr, Ni, Mo, Th, U, and Ba is consistent with hydrothermal input (Li and Gao, 1996). Moreover, significant Ba enrichment of the tuff layer of the Rongxi section suggests that hydrothermal and volcanic activities were coeval. It is plausible, then, that K-feldspar-rich volcanic ash reacted with Ba-rich hydrothermal fluids advecting along deep faults to produce hyalophane and silica within newly deposited sediment.

5.4. Microenvironments of nodule formation

The ready substitution of REE^{3+} for Ca^{2+} in apatite (Kidder et al., 2003) likely accounts for the enriched REE values of phosphorite and phosphate nodules in REE (Zhu et al., 2014; Jiang et al., 2007, and this study). REE compositions of the NTT deposits potentially record the REE pattern of ambient waters during diagenetic formation and can be used to evaluate depositional or diagenetic microenvironments (McArthur and Walsh, 1984; Shields and Still, 2001; Zhu et al., 2014). Jiang S-Y and colleagues have reported on investigations of carbonate and phosphate fractions of phosphate nodules (Jiang et al., 2007; Zhu et al., 2014; Xin et al., 2015; Zhu and Jiang, 2017). They describe a seawater-like REE pattern preserved in the carbonate fraction and a hat-shaped REE pattern recorded in the phosphate fraction, a likely representation of mixed seawater and porewater signatures. Recently, Chen et al. (2015) related the hat-shaped REE pattern to the simultaneous preferential adsorption of light and heavy

REEs to Mn- and Fe-oxyhydroxides, respectively, leaving the residual REE content of porewaters enriched in intermediate REEs. Thus, the hat-shaped REE + Y pattern of the NTT phosphate nodules (Fig. 8A) probably reflects mixed seawater and porewater signatures.

The Ce anomaly can be used as a redox proxy in marine sediments when REE is primarily of hydrogenous origin rather than lithogenous origin (Chen et al., 2015; Zhang et al., 2016). The Y/Ho ratio is quite useful for distinguishing REE of hydrogenous origin from that derived from lithogenous sources. NTT phosphate nodules cluster off the ideal hydrogenous – lithogenous trend of Zhang et al. (2016) on the Y/Ho versus Σ REE crossplot (Fig. 14). Strongly enriched Σ REE levels of the nodules relative to Y/Ho likely reflects the diagenetic addition of REE supplied by hydrogenous components (e.g., OM, Fe-Mn oxyhydroxides) rather than lithogenous sediment (e.g., clay minerals; Chen et al., 2015). Moreover, Y/Ho values of phosphate nodules (> 44 ; Fig. 14) suggest that more than half of their REE content was sourced in seawater. Thus, Ce anomalies are used in the present study to elucidate the early diagenetic environment under which the NTT phosphate nodules formed.

The Pr/Pr* ratio is commonly used in conjunction with the Ce/Ce* ratio because of the possible misrepresentation of negative Ce anomalies that may reflect oxic conditions caused by elevated La contents (Bau and Dulski, 1996). The distribution of phosphate nodule data on the Ce/Ce* versus Pr/Pr* discriminant plot (i.e., genuine negative Ce anomaly suggested by Ce/Ce* < 0.95 and Pr/Pr* > 1.05 ; Shields and Still, 2001) indicates that La concentration had no influence on Ce anomalies of the studied

samples. The negative Ce anomalies documented from CFA of the studied phosphate nodules ($Ce/Ce^* = 0.39-0.46$; Fig. 8A) are consistent with formation under oxic-suboxic microenvironmental conditions (Jiang et al., 2007; Zhu et al., 2014; Zhu et al., 2017).

Figure 14 Near here

Negative Ce anomalies suggest that the NTT phosphate nodules precipitated under oxic-suboxic conditions, an interpretation is at odds with the present and previous investigations relating deposition of the NTT black shale to widespread anoxic or even euxinic conditions (Goldberg et al., 2007; Guo et al., 2007; Och et al., 2013; Gao et al., 2016; Cheng et al., 2016, 2017) (Fig. 9-11). Jiang et al. (2007), citing Ce anomalies < 0.4 in cores of phosphate nodules that increase outward to nodule rims, postulated that phosphate nodules may have grown across redox boundaries. Moreover, a recent LA-ICP-MS mapping analysis of a phosphate nodule hosted by Lower Cambrian black shale suggests that nodule growth is controlled by pore water redox conditions (Zhou et al., 2017). Specifically, nodule growth appears to initiate under oxic pore fluid conditions and is terminated by establishment of an anoxic microenvironment (Zhou et al., 2017). Therefore, it is plausible that the existence of oxygenated pore water soon after deposition resulted in the release of P from aerobically oxidized OM, which triggered precipitation of phosphate. The exhaustion of dissolved oxygen in the pore water environment via aerobic respiration brought nodule growth to an end.

5.5. Proposed model of phosphate nodule formation

Marginal areas of the Yangtze Block received increased fluxes of nutrients during Early Cambrian time (Fig. 15A). The increased flux of nutrients, including river-borne and volcanic, resulted in a bloom of marine plankton. Primary producers included sponges (Fig. 5B and 6E, F), marine algae (e.g., red and green alga), and bacteria (Steiner et al., 2001; Braun et al., 2007). The redox-stratified nature of the ocean at this time (Goldberg et al., 2007; Och et al., 2013; Jin et al., 2016; Cheng et al., 2016, 2017) induced the release of phosphate adsorbed onto FeOOH and contained within OM into the water column. Coastal upwelling of P-rich bottom water increased planktonic productivity in oxygenated surface water and consequent accumulation of phosphorite and carbonaceous shale on the shelf margin (Fig. 15A). Regions of the shelf margin characterized by elevated seawater phosphate concentrations may have been favorable for the formation of NTT phosphate nodules. The postulated formation of the nodules based on our analysis of the Rongxi section is described below:

(1) Marine plankton flourished in the photic zone as a result of the increased input of nutrients. Aerobic oxidation of newly deposited OM released phosphate and dissolved oxygen to pore water leading to the rapid precipitation of crystalline CFA in the nascent nodule core in an oxic microenvironment (Fig. 15B1). Desorption of phosphate from organic matter would have produced gradients of diminishing phosphate away from OM particles.

(2) Continued aerobic bacterial respiration of OM by would have diminished free oxygen content in the sediment thus lowering Eh levels of the microenvironment

(Callow and Brasier, 2009). Consequent oxic-suboxic conditions favored the slow formation of cryptocrystalline CFA overgrowths on previously-formed crystalline CFA (Fig. 6A and 15B2; Li and Schieber, 2015).

(3) Increasing burial depth and continued bacterial oxidation of OM would have further lowered aerobic pH and Eh levels of the microenvironment proximal to the forming phosphate nodules (Callow and Brasier, 2009). Increased acidity favored dissolution of CFA and silica precipitation (Dorozhkin, 2012; Muscente et al., 2015). At minimum pH, K-rich volcanic ash started to react with Ba-rich hydrothermal fluids resulting in the precipitation of hyalophane and quartz. The contemporaneous dissolution of sponge spicules likely contributed to the silica reservoir of this diagenetic environment (Fig. 15B3).

(4) Residual free oxygen was eventually markedly diminished or exhausted by aerobic respiration. Bacterial sulfate reduction (BSR) of OM of the host sediment further lowered the Eh of pore water ($2\text{CH}_2\text{O} + \text{SO}_4^{2-} \rightarrow \text{HCO}_3^- + \text{HS}^- + \text{CO}_2 + 2\text{H}_2\text{O}$; Callow and Brasier, 2009) resulting in the diagenetic formation of pyrite (Fig. 15B4). The continued accumulation of OM resulted in the formation of microbial mats at the sediment-water interface that may have acted as barriers to the diffusion of aqueous phosphate from the sediment thereby maintaining high pore water phosphate concentrations and rapid mineralization (Wilby et al., 1996). Phosphate supersaturation of the pore water environment favored the continued formation of cryptocrystalline CFA overgrowths, which diminished phosphate concentration close to phosphate nodules (Fig. 15B4). Phosphate gradients established within the forming nodules

maintained diffusion of phosphate distant from the nodules until most aqueous phosphate was exhausted via precipitation of the forming nodules or concentration differences reached equilibrium levels, either of which would have diminished nodule growth. However, the transition of the host sediment pore water environment to strongly anoxic (even euxinic) conditions as a result of intense BSR would have suppressed the precipitation of CFA effectively ending nodule growth (Zhou et al., 2017). It is evident, then, that the size of phosphate nodules was a function of the supply of phosphate and microenvironmental redox conditions.

Figure15 Near here

6. Conclusions

Early Cambrian volcanic and hydrothermal events of the Yangtze Block appear to have been critical to the accumulation of NTT organic-rich black shales and the growth of hosted phosphate nodules. A voluminous flux of nutrients, including phosphate, Fe, and Si, to the ocean from volcanic ash and rivers resulted in a marked increase of surface water productivity and the consequent enhanced export of OM to the sea floor. Upwelling of phosphate-enriched bottom water along the shelf margin of the Yangtze Block ultimately fueled widespread phosphogenesis and formation of phosphate nodules.

NTT phosphate nodules consist principally of CFA and display a concentric internal structure that may have been controlled by changing Eh and pH during the

diagenetic history of the nodules and host sediment. Precipitation of CFA is favored by oxic-suboxic pore water microenvironments, although bottom water may have been anoxic-euxinic. To reconcile the co-existence of these contrasting redox conditions, we propose that much of the newly deposited OM contained few amounts of free oxygen under higher primary productivity. The release of dissolved oxygen from the decaying OM created an oxic microenvironment near the sediment-water interface that favored CFA precipitation. The hyalophane-quartz association documented from NTT phosphate nodules may reflect the geochemical interaction of K-feldspar-rich volcanic ash with Ba-rich hydrothermal fluids at the lower pH levels induced by the oxidation of OM. Thus, the NTT phosphate nodules record the complex interaction of enhanced biological productivity and volcanic and hydrothermal activity associated with the E-C transition.

Acknowledgments

Special thanks go to Prof. Thomas Algeo for his kind help with earlier version of manuscript. We also sincerely thank two anonymous reviewers for their insightful comments that greatly improved the manuscript. This work was supported by the National Natural Science Foundation of China (91755211, 41690131), the China Postdoctoral Science Foundation (2018M631688) and the National Science and Technology Major Project of the Ministry of Science and Technology of China (2017ZX05005-001).

References:

- Algeo, T.J., Ingall, E., 2007. Sedimentary C_{org}:P ratios, Paleocyan ventilation, and Phanerozoic atmospheric pO₂. *Palaeogeography, Palaeoclimatology, Palaeoecology* 256, 130-155.
- Algeo, T.J., Lyons, T.W., 2006. Mo-total organic carbon covariation in modern anoxic marine environments: Implications for analysis of paleoredox and paleohydrographic conditions. *Paleoceanography* 21, PA1016.
- Algeo, T.J., Maynard, J.B., 2004. Trace-element behavior and redox facies in core shales of Upper Pennsylvanian Kansas-type cyclothems. *Chemical geology* 206, 289-318.
- Algeo, T.J., Rowe, H., 2012. Paleocyanographic applications of trace-metal concentration data. *Chemical Geology* 324–325, 6-18.
- Algeo, T.J., Tribovillard, N., 2009. Environmental analysis of paleocyanographic systems based on molybdenum–uranium covariation. *Chemical Geology* 268, 211-225.
- Baturin, G.N., 1982. Phosphorites on the Sea Floor. *Developments in Sedimentology*. Elsevier, Amsterdam, 33, pp.343.
- Baturin, G.N., 2003. Phosphorus cycle in the Ocean. *Lithology and Mineral Resources* 38, 101-119.
- Bau, M., Dulski, P., 1996. Distribution of yttrium and rare-earth elements in the Penge and Kuruman iron-formations, Transvaal Supergroup, South Africa. *Precambrian Research* 79(1-2), 37-55.
- Berner, R.A., 1973. Phosphate removal from sea water by adsorption on volcanogenic ferric oxides. *Earth and Planetary Science Letters* 18(1), 77–86.
- Böning, P., Brumsack, H.-J., Böttcher, M.E., Schnetger, B., Kriete, C., Kallmeyer, J., Borchers,

- S.L., 2004. Geochemistry of Peruvian near-surface sediments. *Geochimica et Cosmochimica Acta* 68, 4429-4451.
- Braun, A., Chen, J.-Y., Waloszek, D., Maas, A., 2007. Siliceous microfossils and biosiliceous sedimentation in the lowermost Cambrian of China. Geological Society, London, Special Publications 286, 423-424.
- Callow, R.H.T., Brasier, M.D., 2009. Remarkable preservation of microbial mats in Neoproterozoic siliciclastic settings: Implications for Ediacaran taphonomic models. *Earth-Science Reviews* 96, 207-219.
- Chen, D., Wang, J., Qing, H., Yan, D., Li, R., 2009. Hydrothermal venting activities in the Early Cambrian, South China: Petrological, geochronological and stable isotopic constraints. *Chemical Geology* 258, 168-181.
- Chen, J., Algeo, T.J., Zhao, L., Chen, Z.-Q., Cao, L., Zhang, L., Li, Y., 2015. Diagenetic uptake of rare earth elements by bioapatite, with an example from Lower Triassic conodonts of South China. *Earth-Science Reviews* 149, 181-202.
- Cheng, M., Li, C., Zhou, L., Algeo, T.J., Zhang, F., Romaniello, S., Jin, C.-S., Lei, L.-D., Feng, L.-J., Jiang, S.-Y., 2016. Marine Mo biogeochemistry in the context of dynamically euxinic mid-depth waters: A case study of the lower Cambrian Niutitang shales, South China. *Geochimica et Cosmochimica Acta* 183, 79-93.
- Cheng, M., Li, C., Zhou, L., Feng, L.J., Algeo, T.J., Zhang, F.F., Romaniello, S., Jin, C.S., Ling, H.F., Jiang, S.Y., 2017. Transient deep-water oxygenation in the early Cambrian Nanhua Basin, South China. *Geochimica Et Cosmochimica Acta* 210, 42-58.
- Compston, W., Zhang, Z., Cooper, J.A., Ma, G., Jenkins, R.J.F., 2008. Further SHRIMP

- geochronology on the early Cambrian of South China. *American Journal of Science* 308, 399-420.
- Croxford, N. J. W., Jephcott, S. 1972. The McArthur lead-zinc-silver deposit, N. T. Australian Institute of Mining and Metallurgy Proceedings 243, 1-26.
- Dabard, M.-P., Loi, A., 2012. Environmental control on concretion-forming processes: Examples from Paleozoic terrigenous sediments of the North Gondwana margin, Armorican Massif (Middle Ordovician and Middle Devonian) and SW Sardinia (Late Ordovician). *Sedimentary Geology* 267, 93-103.
- Deer, W.A., Howie, R.A., Zussman, J., 2001. *Rock-Forming Minerals: Feldspars*, vol.4A. Geological Society.
- Dorozhkin, S.V., 2012. Dissolution mechanism of calcium apatites in acids: a review of literature. *World Journal of Methodology* 2, 1-17.
- Dulski, P., 1994. Interferences of oxide, hydroxide and chloride analyte species in the determination of rare earth elements in geological samples by inductively coupled plasma-mass spectrometry. *Fresenius' journal of analytical chemistry* 350, 194-203.
- Elderfield, H., Greaves, M.J., 1982. The rare earth elements in seawater. *Nature* 296, 214-219.
- Föllmi, K.B., 1996. The phosphorus cycle, phosphogenesis and marine phosphate-rich deposits. *Earth-Science Reviews* 40, 55-124.
- Froelich, P.N., Arthur, M.A., Burnett, W.C., Deakin, M., Hensley, V., Jahnke, R., Kaul, L., Kim, K.-H., Roe, K., Soutar, A., Vathakanon, C., 1988. Early diagenesis of organic matter in Peru continental margin sediments: phosphorite precipitation. *Marine Geology* 80, 309-343.

- Froelich, P.N., Klinkhammer, G.P., Bender, M.L., Luedtke, G.R., Heath, G.R., Cullen, D., Dauphin, P., Hammond, D., Hartman, B., Maynard, V., 1979. Early oxidation of organic matter in pelagic sediments of the eastern equatorial Atlantic: suboxic diagenesis. *Geochimica et Cosmochimica Acta* 43, 1075-1090.
- Frondel, C., Ito, J., Hendricks, J. G. 1966. Barium feldspars from Franklin, New Jersey. *American Mineral* 51, 1388-1393.
- Gao, P., Liu, G., Jia, C., Young, A., Wang, Z., Wang, T., Zhang, P., Wang, D., 2016. Redox variations and organic matter accumulation on the Yangtze carbonate platform during Late Ediacaran–Early Cambrian: Constraints from petrology and geochemistry. *Palaeogeography, Palaeoclimatology, Palaeoecology* 450, 91-110.
- Gromet, L.P., Dymek, R.F., Haskin, L.A., Korotev, R.L., 1984. The “North American shale composite”: Its compilation, major and trace element characteristics. *Geochimica et Cosmochimica Acta* 48, 2469-2482.
- Goldberg, T., Strauss, H., Guo, Q., Liu, C., 2007. Reconstructing marine redox conditions for the Early Cambrian Yangtze Platform: Evidence from biogenic sulphur and organic carbon isotopes. *Palaeogeography, Palaeoclimatology, Palaeoecology* 254, 175-193.
- Guo, Q., Strauss, H., Liu, C., Goldberg, T., Zhu, M., Pi, D., Heubeck, C., Vernhet, E., Yang, X., Fu, P., 2007. Carbon isotopic evolution of the terminal Neoproterozoic and early Cambrian: Evidence from the Yangtze Platform, South China. *Palaeogeography, Palaeoclimatology, Palaeoecology* 254, 140-157.
- Han, F., Shen, J., Huchinson, R.W., 1993. Adularia—An important indicator mineral of syngenetic origin for stratiform mineralization at the Dachang tin-polymetallic deposit.

Mineral Deposits 12, 330-337. (in Chinese with English abstract)

- Han, S., Hu, K., Cao, J., Pan, J., Xia, F., Wu, W., 2015. Origin of early Cambrian black-shale-hosted barite deposits in South China: Mineralogical and geochemical studies. *Journal of Asian Earth Sciences* 106, 79-94.
- Jenkins, R.J.F., Cooper, J.A., Compston, W., 2002. Age and biostratigraphy of Early Cambrian tuffs from SE Australia and southern China. *Journal of the Geological Society* 159, 645–658.
- Jin, C., Li, C., Algeo, T.J., Planavsky, N.J., Cui, H., Yang, X., Zhao, Y., Zhang, X., Xie, S., 2016. A highly redox-heterogeneous ocean in South China during the early Cambrian (~529–514Ma): Implications for biota-environment co-evolution. *Earth and Planetary Science Letters* 441, 38-51.
- Jiang, S.Y., Pi, D., Heubeck, C., Frimmel, H., Liu, Y., Deng, H., Ling, H., Yang, J., 2009. Early Cambrian ocean anoxia in South China. *Nature* 459, E5-E6.
- Jiang, S.Y., Zhao, H.X., Chen, Y.Q., Yang, T., Yang, J.H., Ling, H.F., 2007. Trace and rare earth element geochemistry of phosphate nodules from the lower Cambrian black shale sequence in the Mufu Mountain of Nanjing, Jiangsu Province, China. *Chemical Geology* 244, 584-604.
- Kidder, D., Krishnaswamy, R., Mapes, R.H., 2003. Elemental mobility in phosphatic shales during concretion growth and implication for provenance analysis. *Chemical Geology* 198, 335-353.
- Kimura, H., Watanabe, Y., 2001. Oceanic anoxia at the Precambrian-Cambrian boundary. *Geology* 29, 995-998.

- Křibek, B., Hladikova, J., Zak, K., Bendl, J., Pudilova, M., Uhlík, Z., 1996. Barite-hyalophane sulfidic ores at Rožná, Bohemian Massif, Czech Republic: metamorphosed black shale-hosted submarine exhalative mineralization. *Economic Geology* 91, 14-35.
- Li, C., Jin, C., Planavsky, N.J., Algeo, T.J., Cheng, M., Yang, X., Zhao, Y., Xie, S., 2017. Coupled oceanic oxygenation and metazoan diversification during the early-middle Cambrian? *Geology* 45, G39208.1.
- Li, S., Gao, Z., 1996. Silicalite of hydrothermal origin in the Lower Cambrian black rock series of South China. *Acta Mineralogica Sinica* 16,416–422 (in Chinese with English abstract).
- Li, Z., Bogdanova, S., Collins, A.S., Davidson, A., De Waele, B., Ernst, R., Fitzsimons, I.C., Fuck, R., Gladkochub, D., Jacobs, J., 2008. Assembly, configuration, and break-up history of Rodinia: a synthesis. *Precambrian Research* 160: 179-210.
- Li, Y., Schieber, J., 2015. On the origin of a phosphate enriched interval in the Chattanooga Shale (Upper Devonian) of Tennessee-A combined sedimentologic, petrographic, and geochemical study. *Sedimentary Geology*, 329, 40-61.
- Liu, Z.H., Zhuang, X.G., Teng, G.E., Xie, X.M., Yin, L.M., Bian, L.Z., Feng, Q.L., Algeo, T.J., 2015. The Lower Cambrian Niutitang Formation at Yangtiao (Guizhou, SW China): Organic matter enrichment, source rock potential, and hydrothermal influences. *Journal of Petroleum Geology* 38, 411-432.
- Loi, A., Ghiene, J.F., Dabard, M.P., Paris, F., Botquelen, A., Christ, N., Elaouad-Debbaj, Z., Gorini, A., Vidal, M., Videt, B., Destombes, J., 2010. The Late Ordovician glacio-eustatic record from a high-latitude storm-dominated shelf succession: The Bou Ingarf section (Anti-Atlas, Southern Morocco). *Palaeogeography, Palaeoclimatology, Palaeoecology*

296, 332-358.

Ma, P., Wang, L., Wang, C., Wu, X., Wei, Y., 2015. Organic-matter accumulation of the lacustrine Lunpola oil shale, central Tibetan plateau: controlled by the paleoclimate, provenance, and drainage system. *International Journal of Coal Geology* 147-148, 58-70.

McArthur, J.M., Walsh, J.N., 1984. Rare-earth element geochemistry of phosphorites. *Chemical Geology* 47, 191-220.

McLennan, S.M., 1989. Rare earth elements in sedimentary rocks; influence of provenance and sedimentary processes. *Reviews in Mineralogy and Geochemistry* 21, 169-200.

McLennan, S.M., 2001. Relationships between the trace element composition of sedimentary rocks and upper continental crust. *Geochemistry, Geophysics, Geosystems* 2 (2000GC000109, 24 pp.).

Moro, M.C., Cembranos, M.L., Fernandez, A., 2001. Celsian, (Ba, K)-feldspar and cymrite from sedex barite deposits of Zamora, Spain. *Canadian Mineralogist* 39, 1039-1051.

Murray, R.W., Leinen, M., 1993. Chemical transport to the seafloor of the equatorial Pacific Ocean across a latitudinal transect at 135°W: Tracking sedimentary major, trace, and rare earth element fluxes at the Equator and the Intertropical Convergence Zone. *Geochimica et Cosmochimica Acta* 57, 4141-4163.

Muscente, A.D., Hawkins, A.D., Xiao, S., 2015. Fossil preservation through phosphatization and silicification in the Ediacaran Doushantuo Formation (South China): a comparative synthesis. *Palaeogeography, Palaeoclimatology, Palaeoecology* 434, 46-62.

Nelson, G.J., Pufahl, P.K., Hiatt, E.E., 2010. Paleooceanographic constraints on Precambrian phosphorite accumulation, Baraga Group, Michigan, USA. *Sedimentary Geology* 226, 9-

21.

Nozaki, Y., Zhang, J., Amakawa, H., 1997. The fractionation between Y and Ho in the marine environment. *Earth and Planetary Science Letters* 148, 329-340.

Och, L.M., Shields-Zhou, G.A., Poulton, S.W., Manning, C., Thirlwall, M.F., Li, D., Chen, X., Ling, H., Osborn, T., Cremonese, L., 2013. Redox changes in Early Cambrian black shales at Xiaotan section, Yunnan Province, South China. *Precambrian Research* 225, 166-189.

Olgun, N., Duggen, S., Andronico, D., Kutterolf, S., Croot, P.L., Giammanco, S., Censi, P., Randazzo, L., 2013. Possible impacts of volcanic ash emissions of Mount Etna on the primary productivity in the oligotrophic Mediterranean Sea: Results from nutrient-release experiments in seawater. *Marine Chemistry* 152, 32-42.

Paytan, A., Griffith, E.M., 2007. Marine barite: Recorder of variations in ocean export productivity. *Deep Sea Research Part II: Topical Studies in Oceanography* 54, 687-705.

Pedersen, T.F., Calvert, S.E., 1990. Anoxia vs productivity; what controls the formation of organic-carbon-rich sediments and sedimentary rocks? *AAPG Bulletin* 74, 454-466.

Pi, D.-H., Liu, C.-Q., Shields-Zhou, G.A., Jiang, S.-Y., 2013. Trace and rare earth element geochemistry of black shale and kerogen in the early Cambrian Niutitang Formation in Guizhou province, South China: Constraints for redox environments and origin of metal enrichments. *Precambrian Research* 225, 218-229.

Planavsky, N.J., Rouxel, O.J., Bekker, A., Lalonde, S.V., Konhauser, K.O., Reinhard, C.T., Lyons, T.W., 2010. The evolution of the marine phosphate reservoir. *Nature* 467, 1088-1090.

Riegler, T., McClenaghan, S.H., 2017. Authigenic potassic silicates in the Rathdowney Trend,

- southwest Ireland: New perspectives for ore genesis from petrography of gangue phases in Irish-type carbonate-hosted Zn-Pb deposits. *Ore Geology Reviews* 88, 140-155.
- Sawaki, Y., Nishizawa, M., Suo, T., Komiya, T., Hirata, T., Takahata, N., Sano, Y., Han, J., Kon, Y., Maruyama, S., 2008. Internal structures and U–Pb ages of zircons from a tuff layer in the Meishucunian formation, Yunnan province, South China. *Gondwana Research*, 14, 148-158.
- Schoepfer, S.D., Shen, J., Wei, H., Tyson, R.V., Ingall, E., Algeo, T.J., 2015. Total organic carbon, organic phosphorus, and biogenic barium fluxes as proxies for paleomarine productivity. *Earth-Science Reviews* 149, 23-52.
- Scott, C., Lyons, T.W., 2012. Contrasting molybdenum cycling and isotopic properties in euxinic versus non-euxinic sediments and sedimentary rocks: Refining the paleoproxies. *Chemical Geology* 324–325, 19-27.
- Scott, C., Lyons, T.W., Bekker, A., Shen, Y., Poulton, S.W., Chu, X., Anbar, A.D., 2008. Tracing the stepwise oxygenation of the Proterozoic ocean. *Nature* 452, 456-459.
- She, Z., Strother, P., McMahon, G., Nittler, L. R., Wang, J., Zhang, J., Sang, L., Ma, C., Papineau, D., 2013. Terminal Proterozoic cyanobacterial blooms and phosphogenesis documented by the Doushantuo granular phosphorites I: In situ micro-analysis of textures and composition. *Precambrian Research* 235, 20-35.
- Shen, J., Schoepfer, S.D., Feng, Q., Zhou, L., Yu, J., Song, H., Wei, H., Algeo, T.J., 2015. Marine productivity changes during the end-Permian crisis and Early Triassic recovery. *Earth-Science Reviews* 149, 136-162.
- Shen, Y., Schidlowski, M., Chu, X., 2000. Biogeochemical approach to understanding

- phosphogenic events of the terminal Proterozoic to Cambrian. *Palaeogeography, Palaeoclimatology, Palaeoecology* 158, 99-108.
- Shields, G., Stille, P., 2001. Diagenetic constraints on the use of cerium anomalies as palaeoseawater redox proxies: an isotopic and REE study of Cambrian phosphorites. *Chemical Geology* 175, 29-48.
- Steiner, M., Li, G., Qian, Y., Zhu, M., Erdtmann, B.-D., 2007. Neoproterozoic to Early Cambrian small shelly fossil assemblages and a revised biostratigraphic correlation of the Yangtze Platform (China). *Palaeogeography, Palaeoclimatology, Palaeoecology* 254, 67-99.
- Steiner, M., Wallis, E., Erdtmann, B.-D., Zhao, Y., Yang, R., 2001. Submarine-hydrothermal exhalative ore layers in black shales from South China and associated fossils - insights into a Lower Cambrian facies and bio-evolution. *Palaeogeography, Palaeoclimatology, Palaeoecology* 169, 165-191.
- Taylor, S.R., McLennan, S.M., 1985. *The continental crust: Its composition and evolution*. Blackwell Scientific Publications, Oxford, pp. 311.
- Tribovillard, N., Algeo, T.J., Baudin, F., Riboulleau, A., 2012. Analysis of marine environmental conditions based on molybdenum–uranium covariation-Applications to Mesozoic paleoceanography. *Chemical Geology* 324-325, 46-58.
- Tribovillard, N., Algeo, T.J., Lyons, T., Riboulleau, A., 2006. Trace metals as paleoredox and paleoproductivity proxies: An update. *Chemical Geology* 232, 12-32.
- Wang, D., Struck, U., Ling, H.-F., Guo, Q.-J., Shields-Zhou, G.A., Zhu, M.-Y., Yao, S.-P., 2015. Marine redox variations and nitrogen cycle of the early Cambrian southern margin of the

- Yangtze Platform, South China: Evidence from nitrogen and organic carbon isotopes. *Precambrian Research* 267, 209-226.
- Wilby, P.R., Briggs, D.E.G., Bernier, P., Gaillard, C., 1996. Role of microbial mats in the fossilization of soft tissues. *Geology* 24, 787-790.
- Xin, H., Jiang, S.-Y., Yang, J.-H., Wu, H.-P., Pi, D.-H., 2015. Rare earth element and Sr–Nd isotope geochemistry of phosphatic rocks in Neoproterozoic Ediacaran Doushantuo Formation in Zhangcunping section from western Hubei Province, South China. *Palaeogeography, Palaeoclimatology, Palaeoecology* 440, 712-724.
- Xu, L., Lehmann, B., Mao, J., Qu, W., Du, A., 2011. Re–Os age of polymetallic Ni–Mo–PGE–Au mineralization in early Cambrian black shales of South China—a reassessment. *Economic Geology* 106, 511-522.
- Yeasmin, R., Chen, D., Fu, Y., Wang, J., Guo, Z., Guo, C., 2017. Climatic-oceanic forcing on the organic accumulation across the shelf during the Early Cambrian (Age 2 through 3) in the mid-upper Yangtze Block, NE Guizhou, South China. *Journal of Asian Earth Sciences* 134, 365-386.
- Zhang, J., Fan, T., Zhang, Y., Lash, G.G., Li, Y., Wu, Y., 2017. Heterogeneous oceanic redox conditions through the Ediacaran–Cambrian boundary limited the metazoan zonation. *Scientific Reports* 7, 8550.
- Zhang, L., Algeo, T.J., Cao, L., Zhao, L., Chen, Z.-Q., Li, Z., 2016. Diagenetic uptake of rare earth elements by conodont apatite. *Palaeogeography, Palaeoclimatology, Palaeoecology* 458, 176-197.
- Zhou, M., Luo, T., Huang, Z., Long, H., Yang, Y., 2007. Advances in research on K-bentonite.

Acta Mineralogica Sinica 27, 351-359. (in Chinese with English abstract)

Zhou, W., Wang H., Fu, Y., Ye, Y., Wang, X., Su, J., Wang, F., Ge, Z., Liang, H., Wei, S., 2017.

Study on the formation mechanism of phosphate nodules in the early Cambrian period using LA-ICP-MS multi-element imaging technology. *Rock and Mineral Analysis* 36, 97-106. (in Chinese with English abstract)

Zhu, B., Jiang, S-Y., 2017. A LA-ICP-MS analysis of rare earth elements on phosphatic grains of the Ediacaran Doushantuo phosphorite at Weng'an, South China: implication for depositional conditions and diagenetic processes. *Geological Magazine*, 154(6): 1381-1397.

Zhu, B., Jiang, S.Y., Yang, J.H., Pi, D.H., Ling, H.F., Chen, Y.Q., 2014. Rare earth element and Sr-Nd isotope geochemistry of phosphate nodules from the lower Cambrian Niutitang Formation, NW Hunan Province, South China. *Palaeogeography, Palaeoclimatology, Palaeoecology* 398, 132-143.

Zhu, R., Li, X., Hou, X., Pan, Y., Wang, F., Deng, C., He, H. 2009. SIMS U-Pb zircon age of a tuff layer in the Meishucun section, Yunnan, southwest China: Constraint on the age of the Precambrian-Cambrian boundary. *Science in China Series D: Earth Sciences*, 52, 1385-1392.

Figures and Tables:

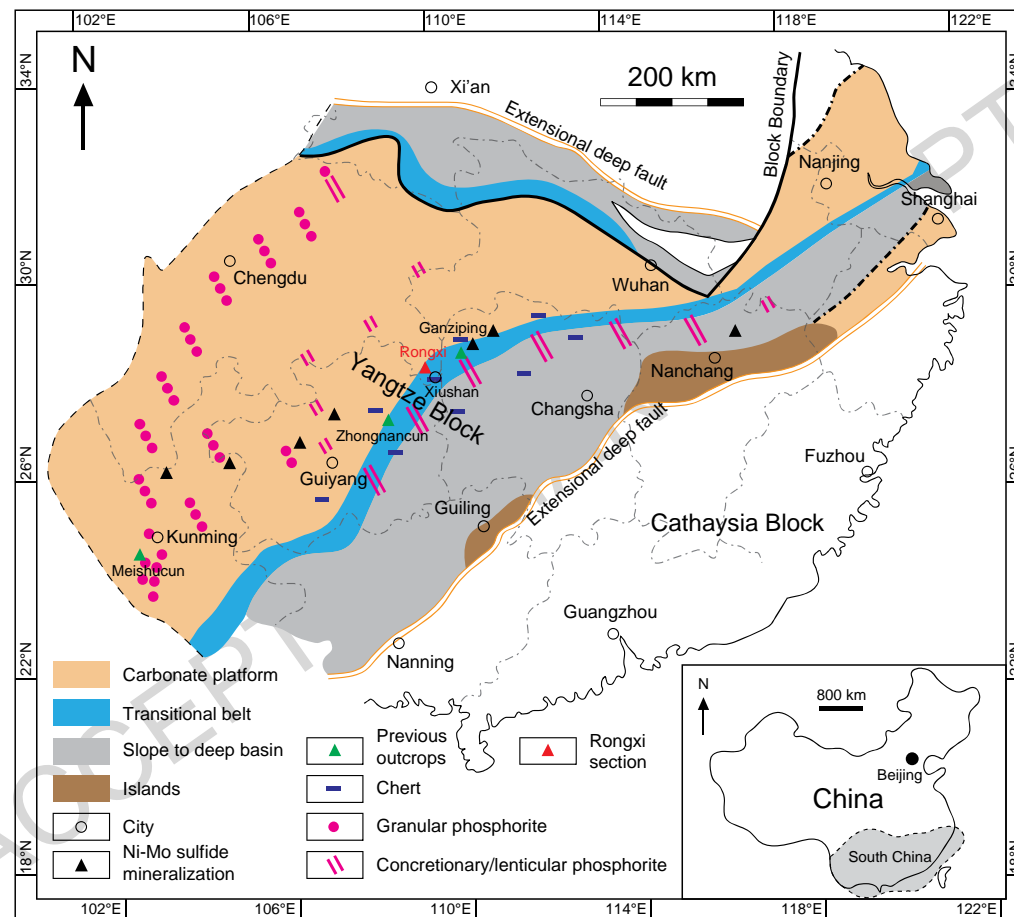


Figure 1. Simplified paleogeographic map showing the Yangtze Block during Early Cambrian time (modified after Chen et al., 2009; Steiner et al., 2001), distribution of chert, granular phosphorites (Steiner et al., 2007) and Ni-Mo sulfide ores (Steiner et al., 2001; Xu et al., 2013).

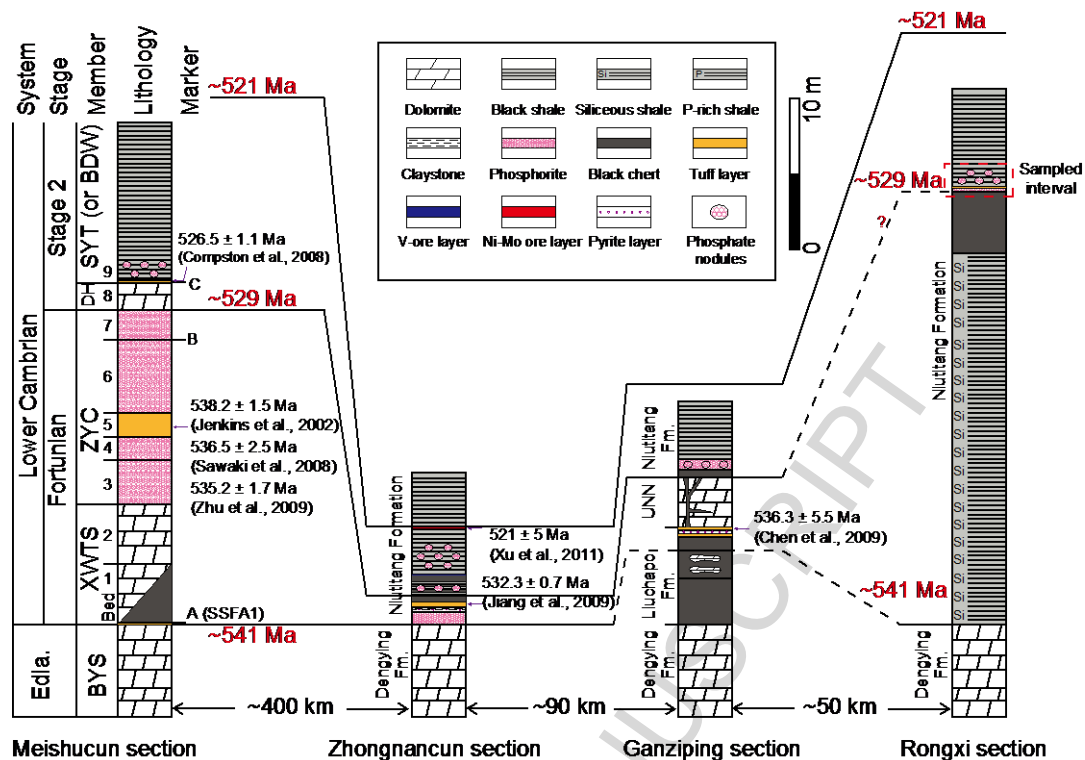


Figure 2. Lithologic columns of the Lower Cambrian Niutitang Formation, including the sampled Rongxi section, the Meishucun section, Yunnan Province (Compston et al., 2008; Zhu et al., 2009; Wang et al., 2015), the Zhongnancun section, Guizhou Province (Pi et al., 2013), and the Ganziping section, Hunan Province (Chen et al., 2009). Locations of these sections are shown in Figure 1. BYS = Baiyanshao; XYTS = Xiaowaitoushan; ZYC = Zhongyicun; DH = Daihai; SYT = Shiyantou; BDW = Baidaowan; UNN = Unnamed.

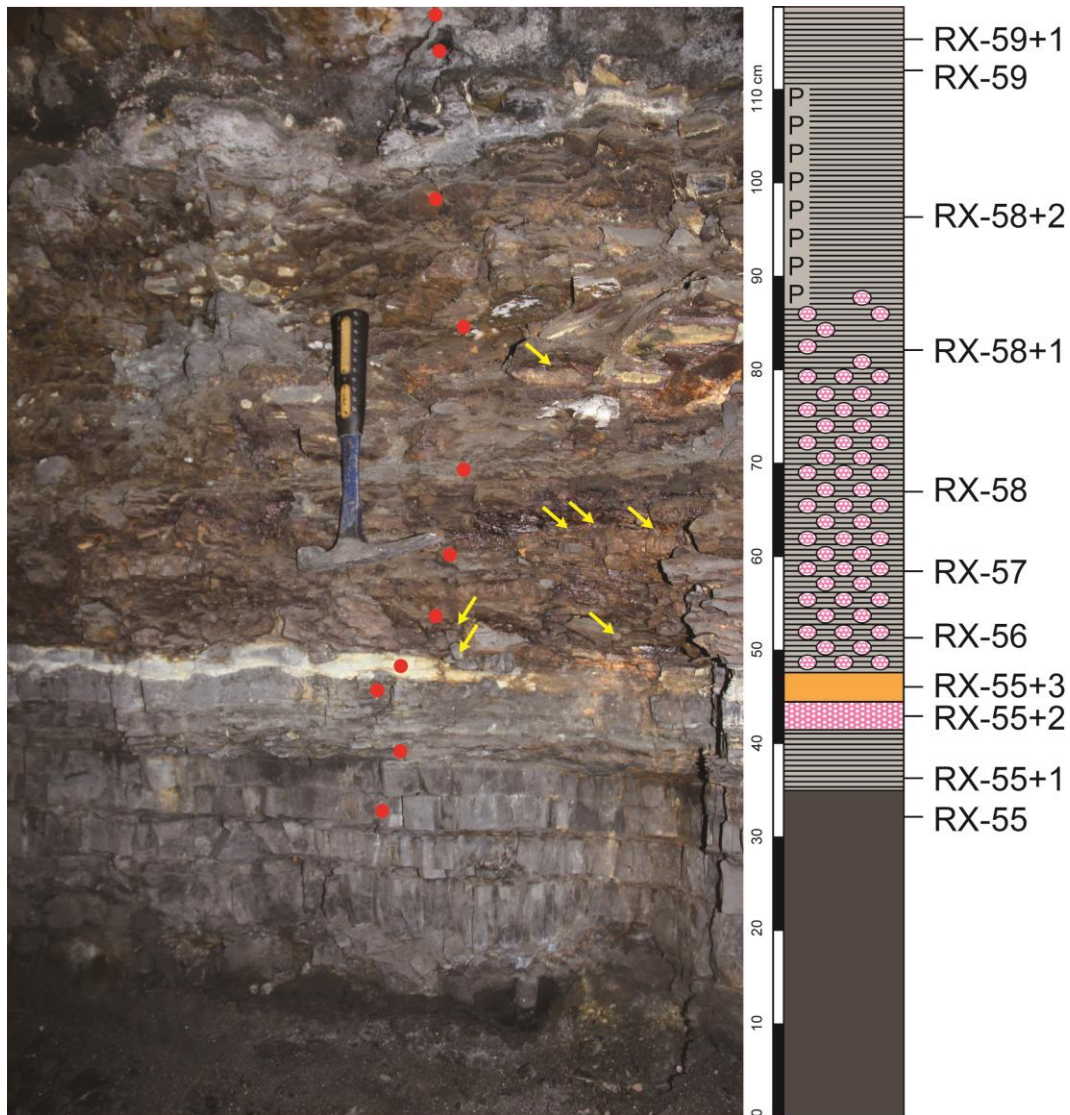


Figure 3. Photograph showing the sampled interval of the Rongxi section and corresponding stratigraphic column. Red points represent sampled locations; yellow arrows indicate phosphate nodules. The geological hammer is 27 cm long. Refer to Figure 2 and Table 1 for lithologic symbols and sample details, respectively.

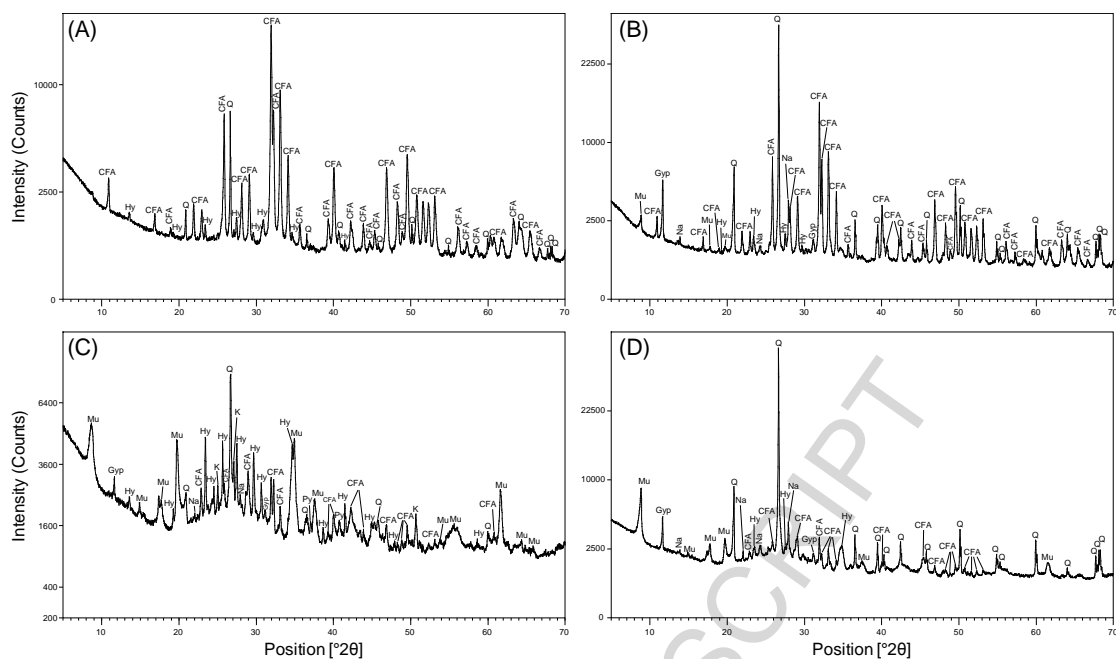


Figure 4. XRD patterns of phosphate nodules and host rocks; (A) RX-071-P1, phosphate nodule; (B) RX-055+2, phosphorite; (C) RX-055+3, tuff layer; (D) RX-056, black shale. Q = quartz; CFA = carbonate fluorapatite; Hy = hyalophane; Mu = Muscovite; Gyp = Gypsum; Na = Albite; K = K-feldspar; Py = Pyrite.

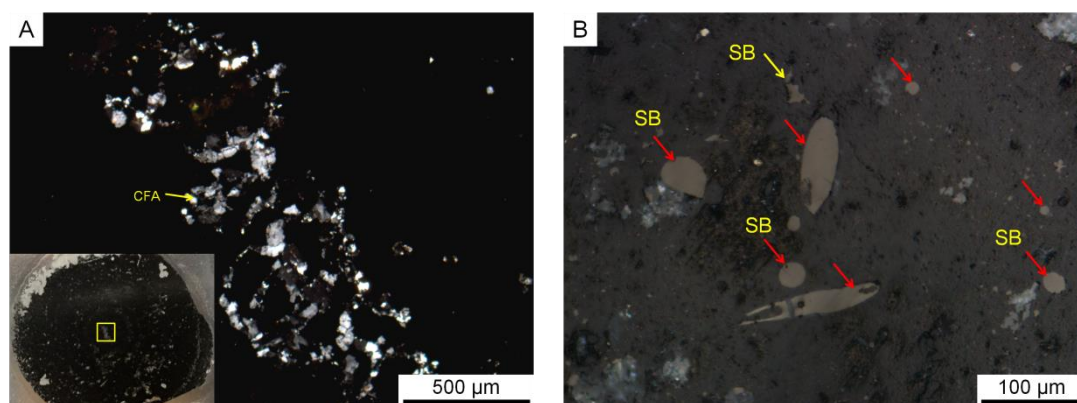


Figure 5. Optical photomicrographs showing textural features of NTT phosphate nodules.

(A) cross-polarized light. The core of nodule consists mainly of crystalline carbonate fluorapatite (CFA); (B) Reflected light. The nodule rim is enriched in solid bitumen (SB), which displays various morphologies, including spherical, elliptical, and rod-like (red arrows), as well as amorphous solid bitumen (yellow arrow).

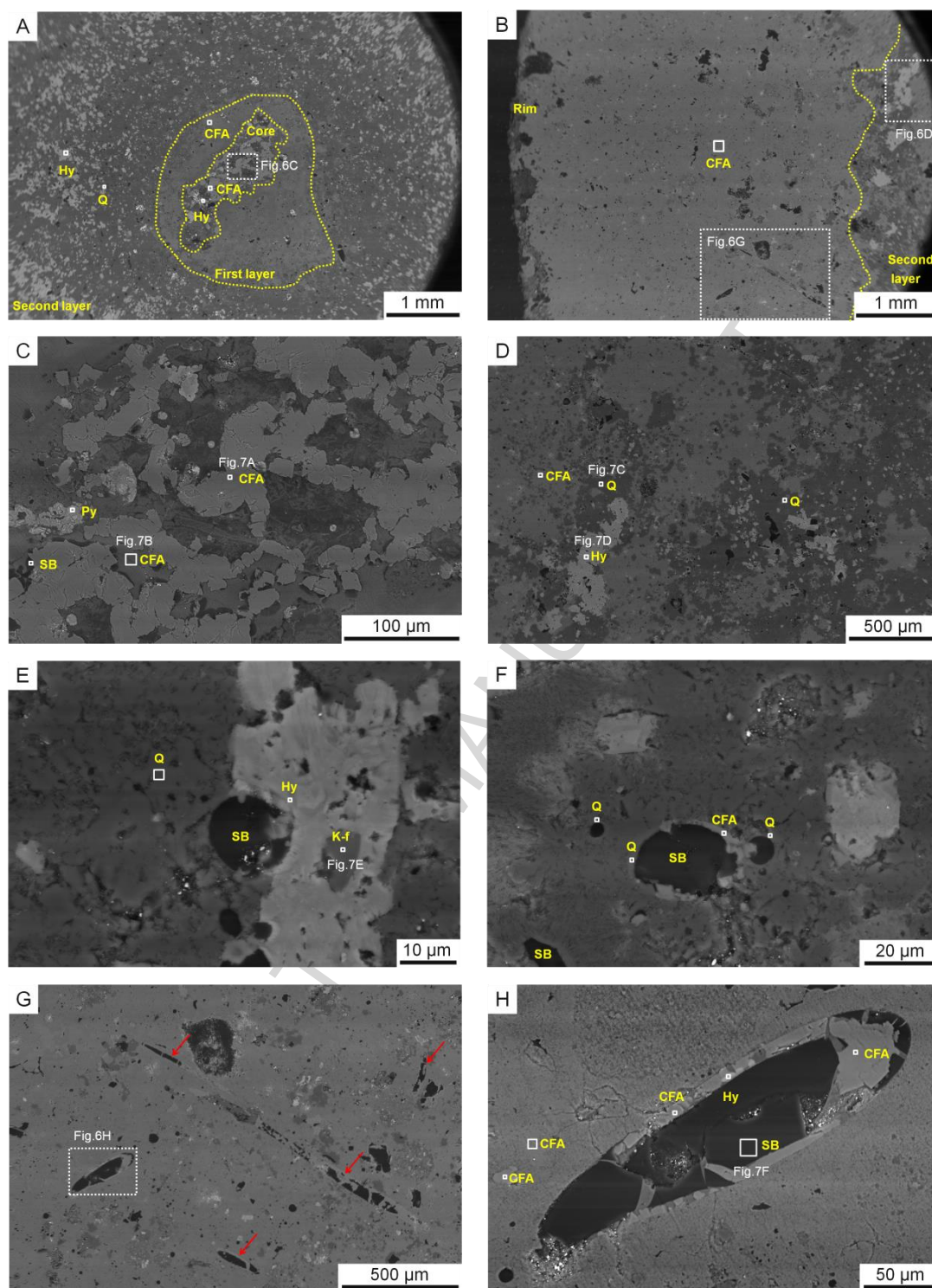


Figure 6. Backscattered electron micrographs showing textures of NTT phosphate nodules. White squares denote areas analyzed by EDS and referred to in Figure 7; **(A, B)** multilayer concentric structure; the core consists mainly of crystalline CFA; the first layer outward from the core consists primarily of cryptocrystalline CFA. The next layer is dominated by hyalophane (Hy) and

quartz (Q); the rim consists mostly of cryptocrystalline CFA; (C) nodule core comprised of abundant CFA (crystalline and cryptocrystalline), SB, and pyrite (Py). SB is concentrated along the edges of crystalline CFA; (D) the Q-Hy association in the first layer outward from the nodule core; cryptocrystalline CFA is found throughout the layer; (E) the association of Hy, K-feldspar (K-f), and Q; (F) microfossil (probably sponge spicule) consisting of two layers. The core is filled with SB, whereas the wall is composed principally of crystalline CFA and Q; (G) nodule rim enriched in needle-like SB (filling sponge spicules?); (H) sponge spicule wall composed mainly of crystalline CFA, and lesser Hy.

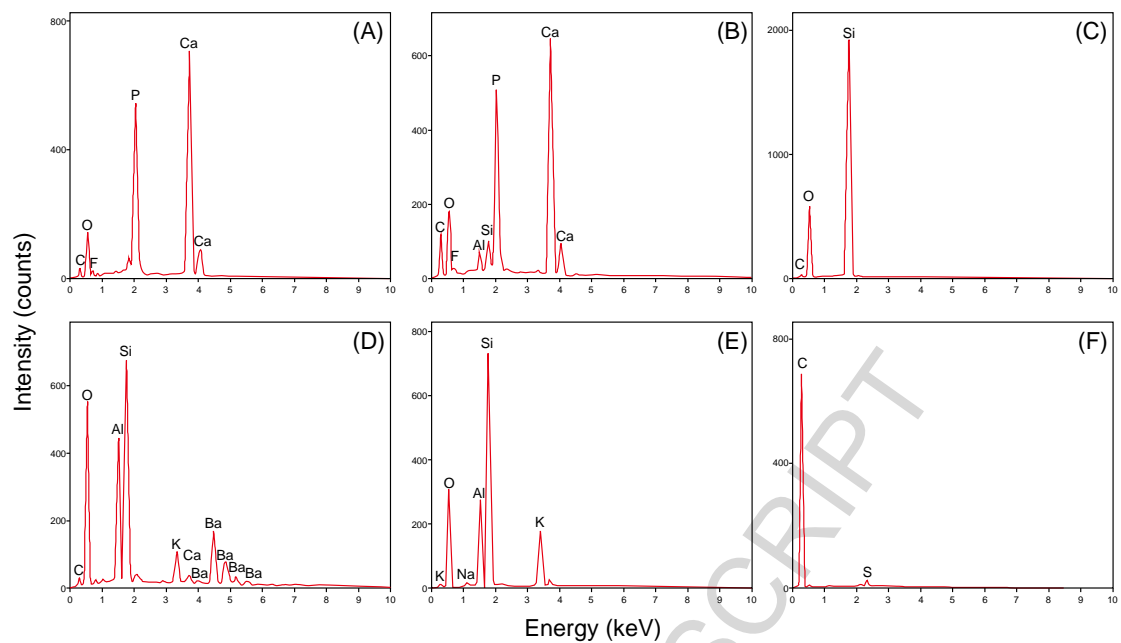


Figure 7. EDS spectra of representative minerals of NTT phosphate nodules. EDS spectra numbers correspond with respective solid red squares in Figure 6; (A) crystalline CFA; (B) cryptocrystalline CFA; (C) quartz; (D) hyalophane (K, Ba); (E) K-feldspar; (F) solid bitumen.

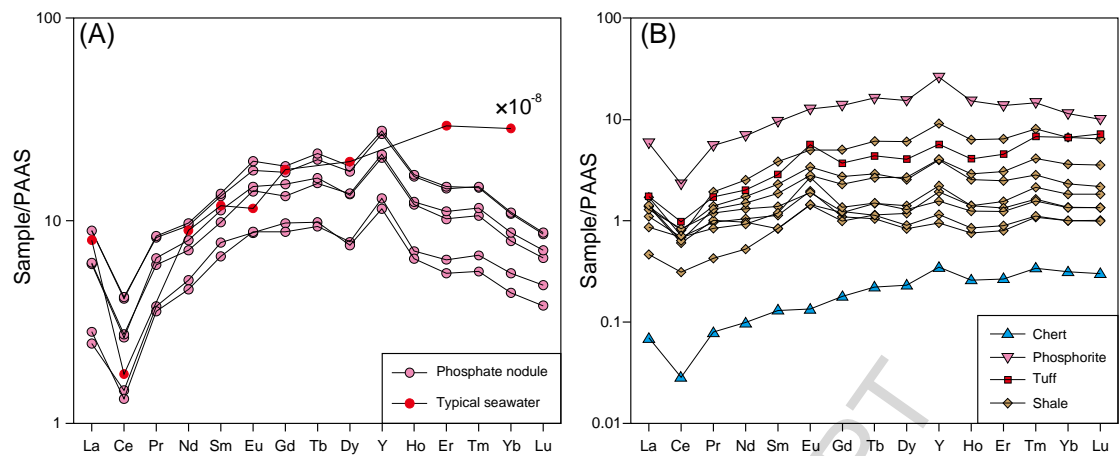


Figure 8. PAAS normalized REE and Y values; (A) NTT phosphate nodules and typical seawater (Elderfield and Greaves, 1982); (B) host rocks of the Rongxi section (PAAS from McLennan, 1989).

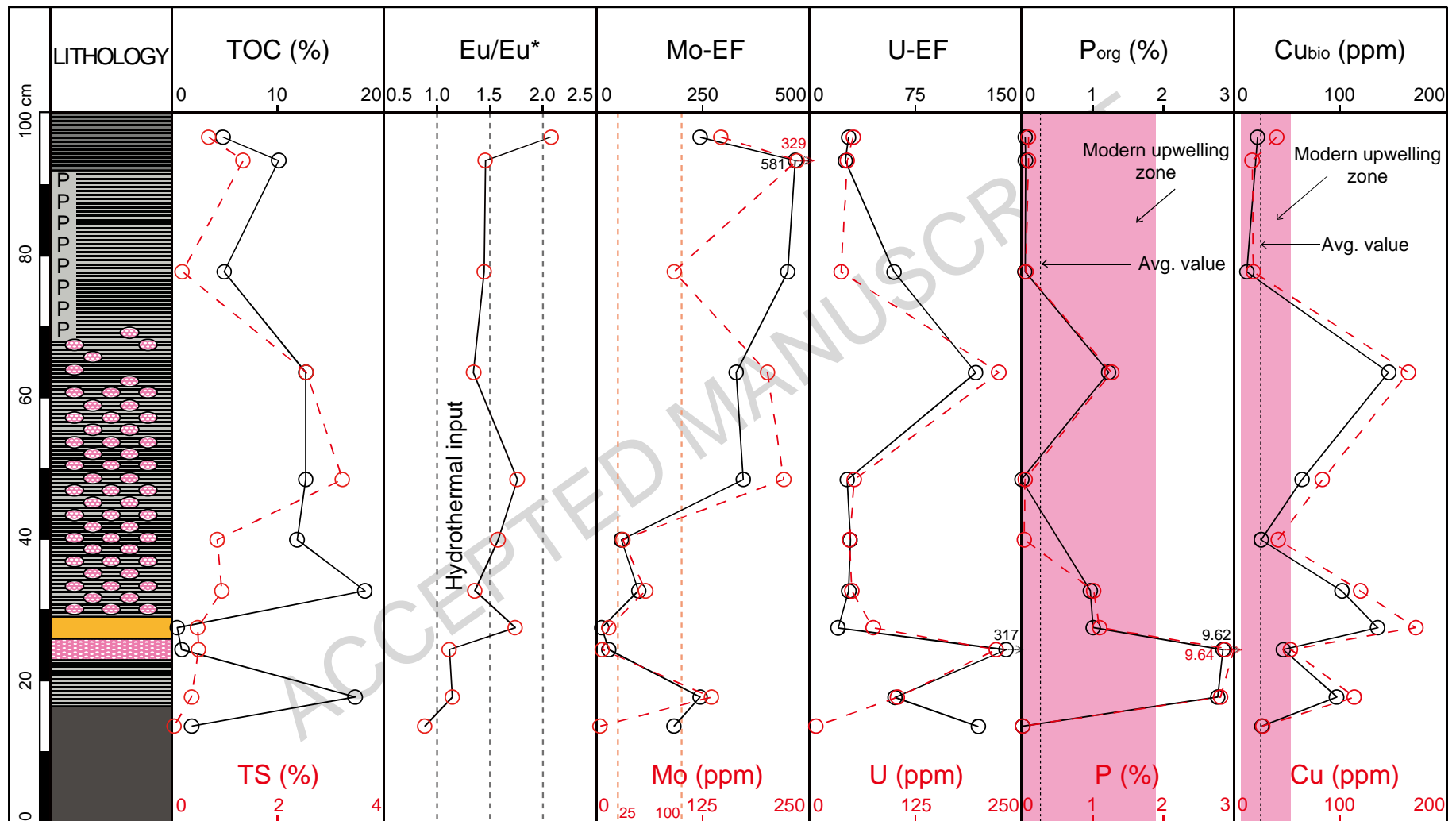


Figure 9. Profiles showing vertical variations of several geochemical proxies. Reference ranges for P_{org} and Cu_{bio} are calculated from sediment recovered from

beneath upwelling zones of the modern equatorial Pacific Ocean (Murray and Leinen, 1993) and off Peru (Böning et al., 2004).

ACCEPTED MANUSCRIPT

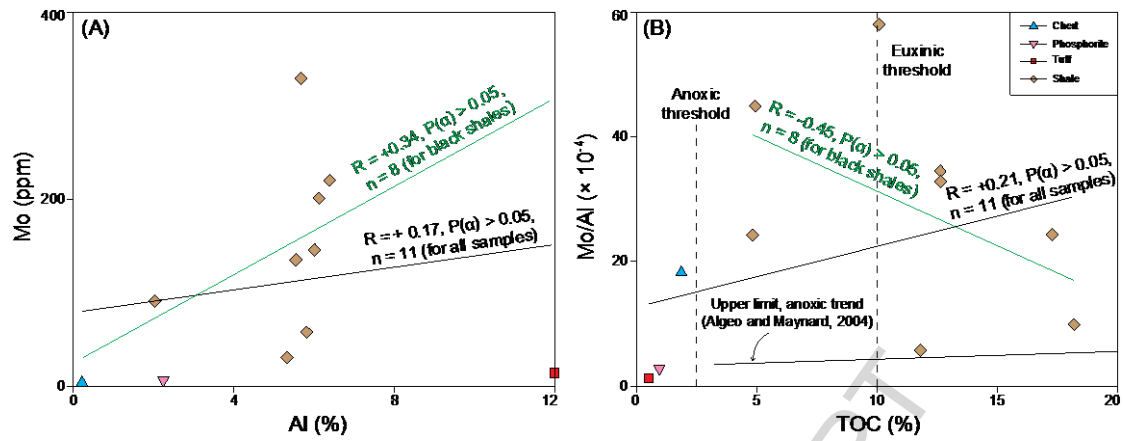


Figure 10. Crossplots of (A) Al versus Mo concentrations and (B) TOC versus Mo/Al of the studied host rocks of the Rongxi section. Anoxic and euxinic thresholds, as well as the anoxic trend proposed by Algeo and Maynard (2004).

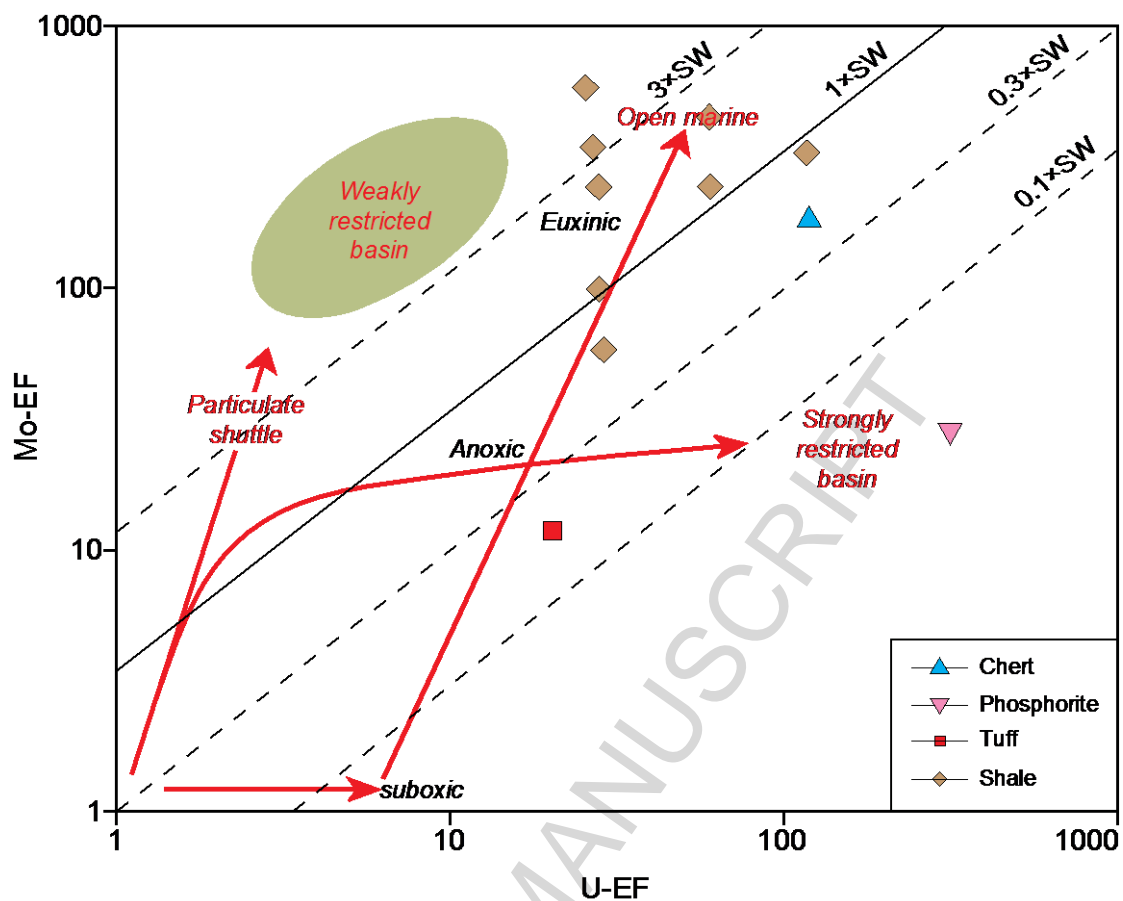


Figure 11. Mo-EF versus U-EF crossplot of Rongxi section samples exclusive of phosphate nodules samples. Diagonal lines represent multiples (0.1, 0.3, 1, and 3) of the Mo:U ratio of present-day seawater. The light-green field represents the “particulate shuttle” trend, characteristic of depositional systems in which intense redox cycling of metal (especially Mn-) oxyhydroxides occurs within the water column (modified from Algeo and Tribovillard, 2009; Tribovillard et al., 2012).

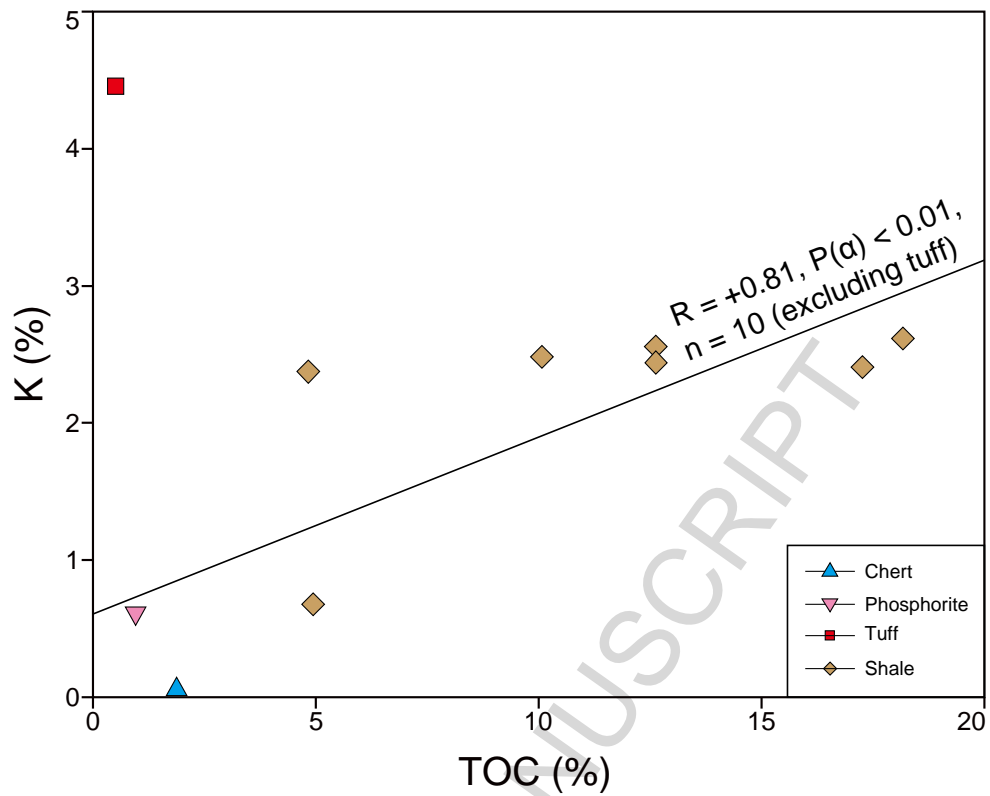


Figure 12. TOC versus K concentration of Rongxi section samples exclusive of phosphate nodules samples. K concentration is calculated from K_2O concentration.

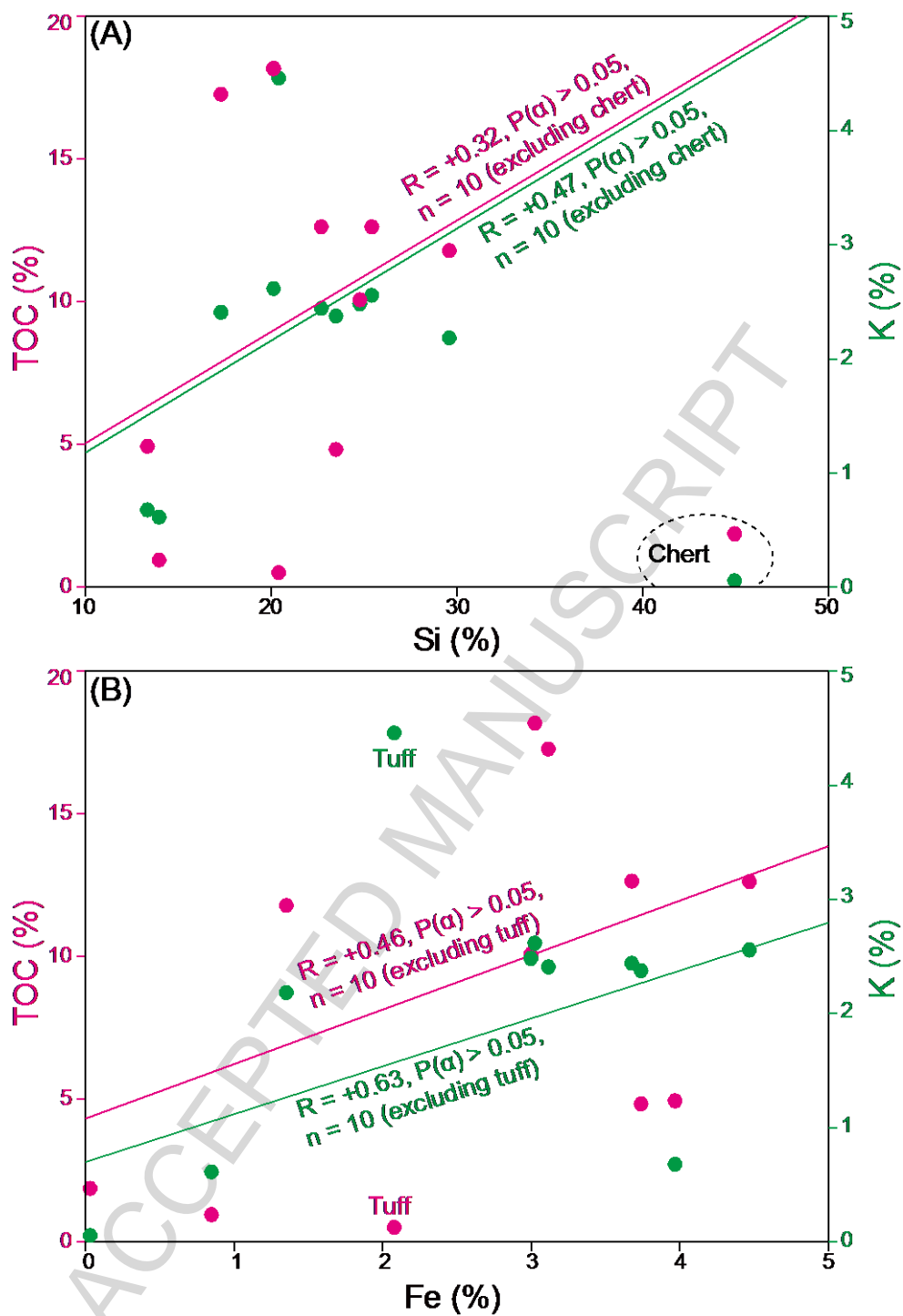


Figure 13. K concentration and TOC versus (A) Si concentration and (B) Fe concentration for shale, phosphorite, tuff, and chert of the Rongxi section. Concentration of major elements (Si, K, and Fe) is calculated from the concentration of major oxides (SiO_2 , K_2O , and $\text{Fe}_2\text{O}_3+\text{FeO}$, respectively).

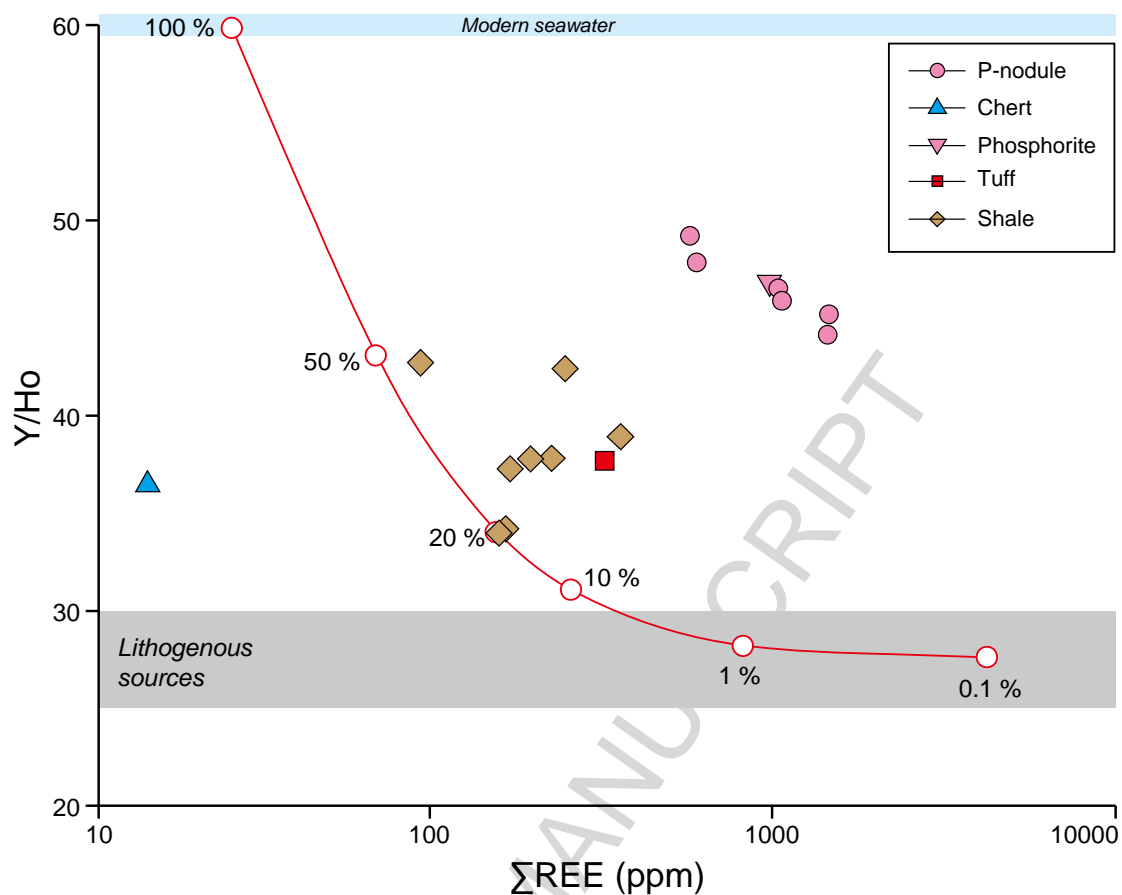


Figure 14. Y/Ho versus Σ REE for NTT phosphate nodules and associated deposits of the Rongxi section. The red curves represent a mixing trend between a hydrogenous (modern seawater) component and a terrigenous (lithogenous) component of an average upper continental crust composition (McLennan, 2001); percentages given as the amount of the hydrogenous component (Chen et al., 2015; Zhang et al., 2016). The majority of REE in phosphate nodules and phosphorite sample (> 50 %) are derived from hydrogenous sources; chert, black shale and tuff samples contain 20-50 % hydrogenous REE.

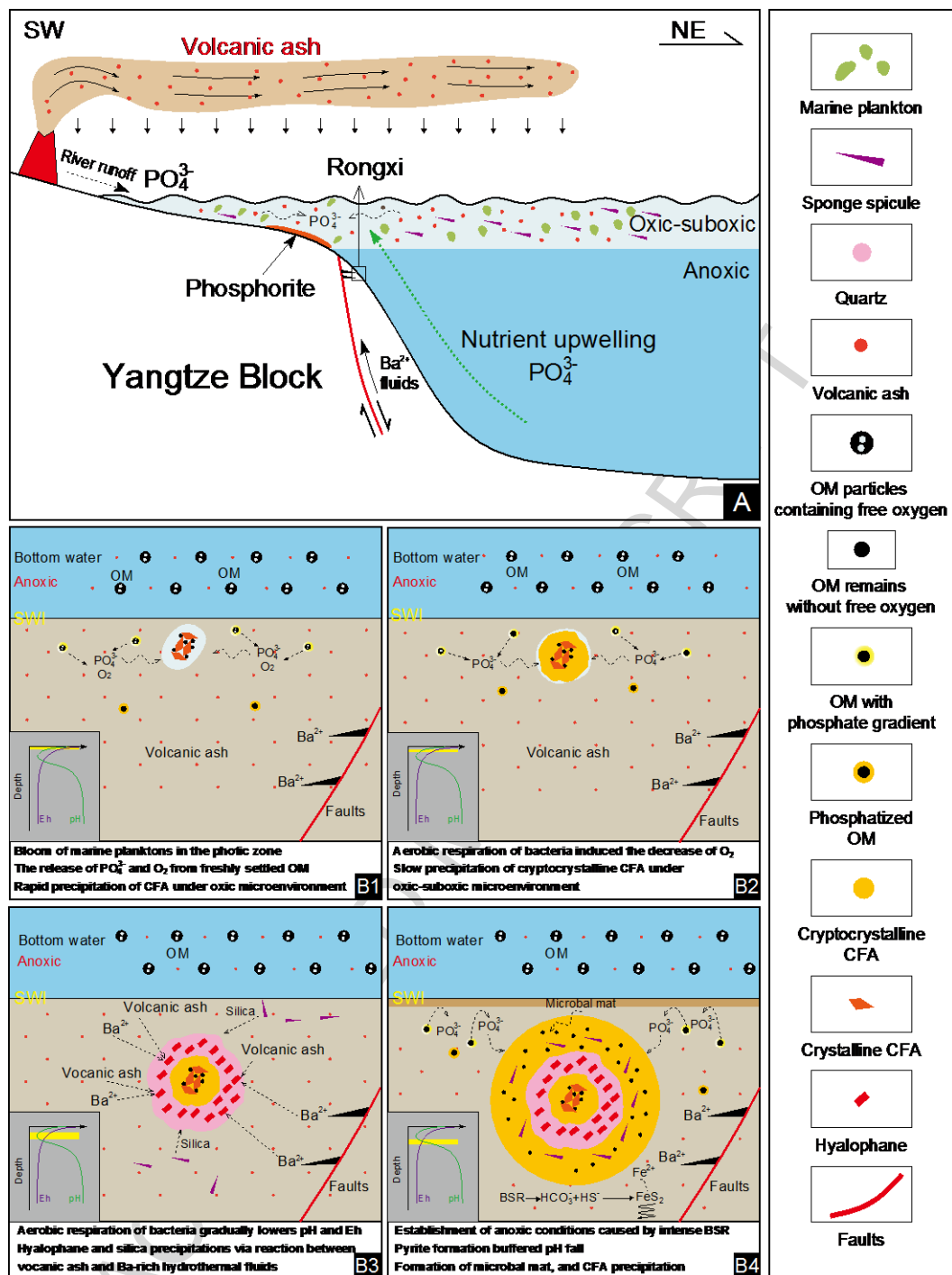


Figure 15. Proposed model for the formation of phosphate nodules in the NTT black shales. Refer to text for discussion.

Tables:

Table 1 Basic information and bulk geochemical parameters of NTT phosphate nodules and host rocks

Sample	Lithology	Size (cm×cm)	TOC (%)	TS (%)
RX-056-P1	Phosphate nodule	3.1×3.4	8.7	0.09
RX-071-P1	Phosphate nodule	2.6×2.7	7.9	0.09
RX-071-P2	Phosphate nodule	2.3×2.3	9.0	0.1
RX-072-P1	Phosphate nodule	2.2×2.7	8.3	0.2
RX-072-P2	Phosphate nodule	2.1×2.3	9.1	0.2
RX-072-P3	Phosphate nodule	1.6×1.8	8.4	0.1
RX-055	Bedded chert		1.9	0.04
RX-055+1	Black shale		17.3	0.4
RX-055+2	Phosphorite		1.0	0.5
RX-055+3	Tuff		0.5	0.5
RX-056	Black shale		18.2	0.9
RX-057	Black shale		11.8	0.9
RX-058	Black shale		12.6	3.2
RX-058+1	Black shale		12.6	2.5
RX-058+2	Black shale		4.9	0.2
RX-059	Black shale		10.1	1.3
RX-059+1	Black shale		4.8	0.7

Table 2 EDS data and calculated molecular formula of hyalophane within the phosphate nodules

Element	C	O	Al	Si	K	Ba	Ca	Molecular formula
	wt.%							
EDS-01	9.1	41.8	9.7	17.4	3.6	18.4	ND	$K_{0.3}Ba_{0.4}Al_{1.1}Si_{1.9}O_8$
EDS-02	ND	43.9	10.9	19.6	3.5	21.4	0.8	$K_{0.3}Ba_{0.5}Al_{1.2}Si_2O_8$
EDS-03	ND	44.8	10.5	19.2	4.3	21.1	ND	$K_{0.3}Ba_{0.4}Al_{1.1}Si_2O_8$
EDS-04	9.6	41.9	9.7	16.4	3.4	19.0	ND	$K_{0.3}Ba_{0.4}Al_{1.1}Si_{1.8}O_8$
EDS-05	11.7	38.5	9.4	15.8	2.2	22.5	ND	$K_{0.2}Ba_{0.5}Al_{1.2}Si_{1.9}O_8$
EDS-06	10.0	41.0	10.0	17.1	2.9	19.0	ND	$K_{0.2}Ba_{0.4}Al_{1.2}Si_{1.9}O_8$
EDS-07	11.0	41.8	8.1	20.3	5.8	10.9	2.3	$K_{0.3}Ba_{0.5}Al_{1.2}Si_{2.1}O_8$
EDS-08	8.5	39.6	10.1	18.1	3.8	19.9	ND	$K_{0.3}Ba_{0.3}Al_{1.0}Si_{2.0}O_8$

ND, not detected.

Table 3 Major element concentrations for NTT phosphate nodules

Sample	Fe	Al	K	Na	Ca	Mg
	%					
RX-056-P1	0.5	0.3	0.09	0.07	33.1	0.1
RX-071-P1	0.1	0.6	0.2	0.2	32.1	0.3
RX-071-P2	0.2	0.3	0.09	0.1	30.5	0.3
RX-072-P1	0.3	0.3	0.1	0.04	31.9	0.4
RX-072-P2	0.3	0.9	0.3	0.1	30.1	0.08
RX-072-P3	0.1	0.2	0.07	0.03	32.8	0.5

Table 4 Concentrations of major element oxides for host rocks

Sample	SiO ₂	Al ₂ O ₃	Fe ₂ O ₃	MgO	CaO	NaO	K ₂ O	MnO	TiO ₂	P ₂ O ₅	FeO	LOI	SUM
	%												
RX-055	96.2	0.4	0.04	0.07	0.1	0.02	0.07	0.004	0.01	0.04	<0.1	2.4	99.4
RX-055-1	37.0	10.5	2.6	1.2	8.2	0.06	2.9	<0.004	0.4	6.4	1.7	23.8	94.8
RX-055-2	29.9	4.2	0.6	0.3	30.3	0.5	0.7	<0.004	0.06	22.1	0.5	7.3	96.5
RX-055-3	43.7	22.7	2.4	2.0	3.0	0.4	5.4	<0.004	0.6	2.5	0.6	9.3	92.3
RX-056	43.0	11.0	2.2	1.3	3.7	0.6	3.2	<0.004	0.6	2.3	1.9	25.3	95.2
RX-057	63.3	10.0	1.0	1.1	0.1	0.8	2.6	<0.004	0.6	0.09	0.8	15.6	96.2
RX-058	54.4	12.1	4.6	1.0	0.6	1.3	3.1	<0.004	0.8	0.1	1.6	16.5	96.1
RX-058-1	48.6	11.6	3.8	1.1	4.1	1.2	2.9	<0.004	0.7	2.9	1.4	17.8	96.0
RX-058-2	28.5	3.8	4.4	10.3	16.8	0.5	0.8	0.391	0.2	0.1	1.1	30.6	97.6
RX-059	53.0	10.7	3.4	0.7	2.2	1.8	3.0	<0.004	0.8	0.2	0.8	15.5	92.2
RX-059-1	50.2	11.4	4.4	2.5	7.2	1.5	2.9	0.08	0.8	0.2	0.9	14.5	96.6

LOI, loss on ignition, largely reflects carbon dioxide (CO₂) from carbonate minerals.

Table 5 Selected trace element concentrations and associated parameters for NTT phosphate nodules and host rocks

Sample	V	Cr	Ni	Mo	Th	U	Ba	Cu	Zn	Ni	Mo/Al	P _{org}	Cu _{bio}	EF-U	EF-Mo
	ppm										ppm/%	%	ppm		
RX-056-P1	509	94.7	53.1	16.5	1.65	64.3	660	97.6	98.0	53.1	58.7	NA	NA	739	588
RX-071-P1	176	90.2	43.1	4.94	4.64	52.3	7550	24.3	52.5	43.1	8.05	NA	NA	275	80.5
RX-071-P2	157	81.7	52.4	5.53	4.11	71.7	1790	149	321	52.4	20.3	NA	NA	851	204
RX-072-P1	485	67.0	50.0	9.95	4.29	116	1570	83.5	2000	50.0	31.2	NA	NA	1170	312
RX-072-P2	158	102	67.1	15.6	7.59	80.5	13800	45.4	114	67.1	16.6	NA	NA	277	166
RX-072-P3	185	129	53.7	2.88	3.06	86.0	1440	29.7	133	53.7	14.1	NA	NA	1360	141
RX-055	91.4	96.9	16.6	3.91	0.35	7.97	466	26.8	16.6	22.3	18.2	0.02	26.2	119	182
RX-055-1	6400	4360	117	135	8.43	104	8970	113	117	186	24.3	2.77	96.4	60.6	244
RX-055-2	969	470	25.2	6.38	2.16	220	7170	53.0	25.2	149	2.84	9.62	46.3	317	28.5
RX-055-3	3070	96.3	70.2	14.2	51.3	75.4	46500	171	70.2	242	1.18	1.01	135	20.3	11.9
RX-056	3640	3760	132	57.5	8.70	50.4	13000	119	132	233	9.89	0.97	102	28.0	99.0
RX-057	4340	2300	86.6	30.8	7.30	47.6	11500	41.5	86.6	82.9	5.79	0	25.6	28.9	58.0
RX-058	4700	228	291	220	10.2	53.0	16500	83.1	291	395	34.5	0.004	64.0	26.8	345
RX-058-1	7570	262	319	201	10.0	223	13700	164	319	637	32.8	1.23	146	118	329
RX-058-2	528	30.9	837	91.2	2.51	37.7	4000	18.2	837	2050	44.9	0.05	12.1	59.9	449
RX-059	1590	103	199	329	10.5	44.8	21300	17.0	199	76.3	58.0	0.06	0	25.5	581
RX-059-1	949	87.6	231	146	9.73	52.0	22100	40.0	231	266	24.3	0.05	22.0	27.9	243
PAAS ^a	150	110	55.0	1.00	14.6	3.10	650	50.0	85.0	55.0	0.10	-	-	-	-
Non-hydrothermal sediments ^b	-	38.0	14.8	7.9	3.2	-	149	-	259	14.8	-	-	-	-	-
Hydrothermal sediments ^b	-	69.1	23.9	12.3	3.4	14.0	1080	-	2040	23.9	-	-	-	-	-

^a, PAAS from Taylor and McLennan, 1985. ^b, Non-hydrothermal and hydrothermal sediments from Li and Gao, 1996.

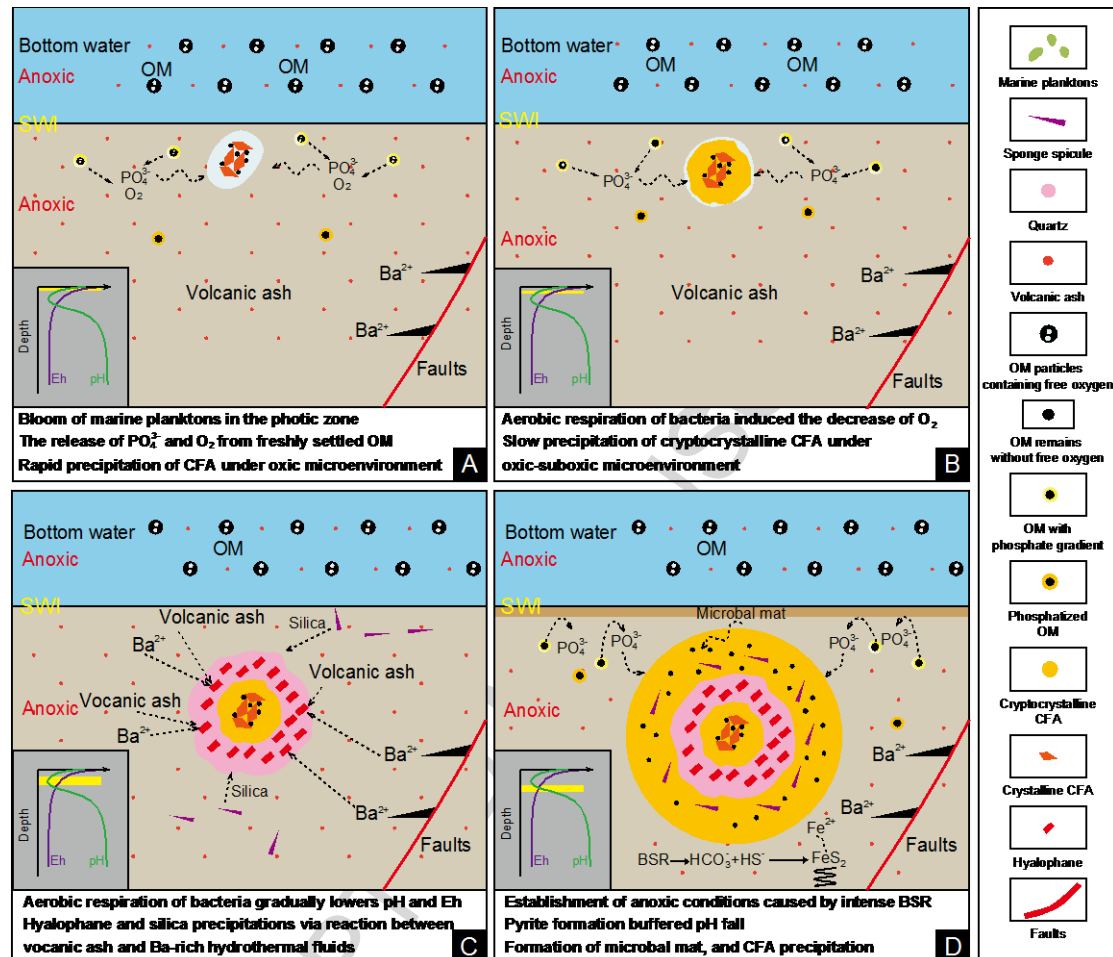
Table 6 REE concentrations and associated parameters for NTT phosphate nodules and host rocks.

Sample	La	Ce	Pr	Nd	Sm	Eu	Gd	Tb	Dy	Ho	Er	Tm	Yb	Lu	Y	Σ REE	Y/Ho	Ce/Ce*	Eu/Eu*	Pr/Pr*
	ppm																			
RX-056-P1	108	106	31.4	155	36.9	9.50	41.1	6.9	36.7	7.00	18.3	2.70	15.4	2.10	344	577	49.2	0.39	1.15	1.20
RX-071-P1	343	329	74.8	331	76.2	21.5	86.7	16.0	87.9	16.7	41.9	5.90	30.6	3.80	755	1470	45.2	0.45	1.25	1.22
RX-071-P2	239	221	54.1	244	55.3	15.3	62.4	11.4	64.2	12.4	31.9	4.70	25.0	3.00	577	1040	46.5	0.42	1.23	1.23
RX-072-P1	95.9	118	33.9	174	43.6	9.50	45.9	7.40	35.9	6.50	15.9	2.30	12.6	1.70	312	603	47.9	0.44	1.00	1.16
RX-072-P2	344	339	73.2	324	74.0	19.2	81.4	14.9	82.6	16.4	41.4	6.00	31.4	3.80	724	1450	44.2	0.46	1.16	1.20
RX-072-P3	233	212	57.9	272	61.8	15.8	70.3	11.9	62.4	11.9	28.9	4.30	22.4	2.80	546	1067	45.9	0.40	1.13	1.23
RX-055	2.72	2.31	0.71	3.40	0.70	0.10	0.80	0.17	1.10	0.26	0.76	0.14	0.88	0.13	9.40	14.3	36.5	0.36	0.88	1.25
RX-055-1	66.1	58.2	17.3	86.8	21.5	5.40	23.6	4.60	28.4	6.30	18.4	3.30	19.0	2.80	246	362	38.9	0.36	1.14	1.19
RX-055-2	219	182	48.2	230	52.0	13.4	62.5	11.8	70.3	14.8	38.7	5.90	31.5	4.30	693	984	46.8	0.38	1.11	1.20
RX-055-3	65.3	76.8	14.9	67.1	15.6	6.00	16.9	3.20	18.6	4.00	12.7	2.70	18.3	3.03	150	325	37.7	0.54	1.73	1.15
RX-056	53.6	49.9	11.3	50.7	10.2	3.00	10.5	1.90	12.3	2.80	8.60	1.60	10.0	1.50	107	228	37.8	0.44	1.35	1.21
RX-057	52.5	48.3	8.80	32.6	4.70	1.50	4.60	0.85	5.50	1.40	4.50	0.86	5.20	0.79	52.2	172	37.3	0.49	1.57	1.27
RX-058	42.4	55.2	8.60	35.7	6.40	2.10	5.20	0.78	3.90	0.80	2.30	0.44	2.90	0.44	26.0	167	34.2	0.64	1.75	1.12
RX-058-1	52.7	64.3	12.3	58.8	12.7	3.60	12.7	2.10	11.8	2.50	7.00	1.13	6.50	0.93	106	249	42.4	0.54	1.34	1.10

RX-058-2	17.7	24.8	3.80	17.8	4.70	1.60	5.60	1.10	6.60	1.40	3.90	0.68	4.00	0.60	59.8	94.1	42.7	0.64	1.44	1.02
RX-059	49.1	65.8	10.5	44.5	7.70	2.10	5.70	0.80	4.20	0.80	2.50	0.46	2.80	0.43	31.1	198	37.8	0.64	1.45	1.11
RX-059-1	33.2	55.2	7.40	31.4	6.60	2.80	6.30	1.10	6.00	1.20	3.50	0.63	3.80	0.58	41.8	160	34.0	0.78	2.07	1.04

ACCEPTED MANUSCRIPT

Graphical Abstract



Highlights

- (1) Phosphate nodules display a concentric structure that may be controlled by changing Eh and pH during the diagenesis.
- (2) Discovery of hyalophane-quartz associations in phosphate nodules reflects possible interaction of volcanic ash and Ba-rich hydrothermal fluids.
- (3) Volcanic and hydrothermal activities appear to be critical to the formation of organic-rich black shales and phosphate nodules during the E-C transition.